Global quantitative understanding of yeast's fate decision making in response to sexual deception

Sheng Li[1, 2], Qiong Liu[2, *], Erkang Wang[1, 2], Jin Wang[3, *]

[1]College of Chemistry, Jilin University, Changchun, Jilin, 130012 P. R. China; [2]State Key Laboratory of Electroanalytical Chemistry, Changchun Institute of Applied Chemistry, Chinese Academy of Sciences, Changchun, Jilin, 130022, China; [3]Department of Chemistry and of Physics and astronomy, State University of New York at Stony Brook, Stony Brook, New York, 11794-3400, USA.

[*] For correspondence: liuqiong@ciac.ac.cn (QL); jin.wang.1@stonybrook.edu (JW).

Abstract

Cell cycle arrest and polarized cell growth are commonly used to qualitatively characterize the yeast's fate in response to sexual deception. Biologically, the cellular decisions governing these fates can be viewed as cascading signals along response pathways. However, it is unknown how quantitatively the cell fate decision-making evolves over time during the macroscopic and microscopic overall response. Here, by observing multi-dimensional responses at the single-cell level, we find that yeast cells can take on a variety of destinies. Multiple states are revealed, along with kinetic

switching rates and pathways among them, giving rise to a quantitative landscape of mating response. The applications of landscape and flux theory to such biological systems enable us to quantify the non-equilibrium dynamics of the yeast cell's mating responses. Furthermore, our experimental results establish the first global quantitative demonstration and understanding of the molecular mechanisms underlying the formation of these states, supporting the real-time synchronization of intracellular signaling with their physiological growth and morphological functions. To further elucidate these microscopic mechanisms, we conduct biochemical reaction simulations to demonstrate the emergence of these states. These findings provide new insights into the global signaling mechanisms underlying how the yeast "think" and do in response to sexual deception.

Introduction

Facing many different external stimuli, cells integrate information from different sources and take appropriate stress responses, such as living or death, division or differentiation, shape change, migration, etc. **(Berg and Brown, 1972; De Oliveira et al., 2016; Kedrin et al., 2007; Kőhidai, 1999; Levine and Rappel, 2013; Macnab and Koshland, 1972; Sourjik and Wingreen, 2012; Vladimirov and Sourjik, 2009; Xu et al., 2016; Yuan et al., 2010; Zhou et al., 2021)**. To better understand the cellular response to external stimuli, we chose the pheromone pathway of Saccharomyces cerevisiae, which was a classic model of mitogen-activated protein kinase (MAPK) signaling pathway for this study **(Chen and Thorner, 2007; Gustin et al., 1998; Slessareva and Dohlman, 2006; Wang and Dohlman, 2004)**. As known, Saccharomyces cerevisiae has two modes of reproduction, sexual mating reproduction and asexual budding reproduction **(Herskowitz, 1988; Hull et al., 2000; Norris and Osley, 1987; Warringer et al., 2011; Zörgö et al., 2013)**. These two reproductive modes can be converted either with or without the assistance of a mate's external pheromone stimulation **(Haber, 2012)**. For the sexual reproduction, mating into diploid is a natural behavior of heterosexual haploid Saccharomyces cerevisiae to cope with unfavorable environment to improve their survival rate for generations **(Bao et al., 2004; Jenness et al., 1983; Youk and Lim, 2014a)**. The mating communication between them is realized by the pheromones, a secreted sex hormone, to inform its spouse to prepare for the start of the cell fusion **(Bao *et al.*, 2004; Bardwell, 2005; Jenness *et al.*, 1983; Marsh and Rose, 1997; Molk and Bloom,**

58 **2006; Rose, 1996; White and Rose, 2001; Youk and Lim, 2014b; Youk and Lim,**
59 **2014a)**. What will happen to the yeast cell if its spouse does not arrive and this
60 normal stimulation continues? From the microscopic internal activities **(Figure 1)**, the
61 external signals are transmitted to Fus3p through a series of internal proteins such as
62 prototype heterotrimeric GTP binding protein and the MAPK kinase cascades
63 **(Dohlman and Thorner, 2001; Errede et al., 1993; Neiman and Herskowitz,**
64 **1994)**. Then, the Fus3p shuttles back and forth across the nuclear membrane, directly
65 or indirectly activating the genes for cell cycle arrest (Far1p) and polar growth
66 (Bni1p) **(Anne-Christine Butty, 1998; Blackwell et al., 2003; Elion et al., 1993;**
67 **Elion et al., 1991; Herskowitz, 1995; Matheos et al., 2004; Peter et al., 1993;**
68 **Roberts and Fink, 1994; van Drogen et al., 2001)**. Thus, current thinking about the
69 responsive fate of the yeast cells encountering sexual deception can be qualitatively
70 summarized as the occurrence of the cell cycle arrest and the polarized cell growth
71 **(Chang and Herskowitz, 1990; Segall, 1993; Shimada et al., 2000)**.
72 While studying qualitatively the fates of cells, researchers realized that, in the
73 presence of many potential external stimuli, the decision-making of the cells can play
74 a central role in the fates of the cells **(Colman-Lerner et al., 2005a; Colman-Lerner**
75 **et al., 2005b; Fang et al., 2018a; Fang et al., 2018b; Gordley et al., 2016; Jiang et**
76 **al., 2019a; Jiang et al., 2019b; St-Pierre and Endy, 2008; Takizawa et al., 1997;**
77 **Zeng et al., 2010)**. Biologically, the cell fate decisions can also be qualitatively
78 described by the cascading transmission of the signals along the static causal pathway
79 **(Bar-Joseph et al., 2012; Behar et al., 2008; Doncic et al., 2015; Hasty et al., 2001;**

80 **Yosef and Regev, 2011)**. However, it is unknown how quantitatively the cell fate
81 decision-making evolves over time during the overall response at both macroscopic
82 and microscopic levels. Since the living cell itself is a complex non-equilibrium micro
83 system, the disturbances of the external environment undoubtedly break the original
84 balance of the yeast cells and exacerbate the imbalance of the internal activities
85 **(Balázsi et al., 2011; Davidson and Erwin, 2006; Feng and Wang, 2011; Li and**
86 **Wang, 2014; Van Kampen, 1992; Wang et al., 2010a; Wang et al., 2008a; Wang et**
87 **al., 2008b; 2010b; Wang et al., 2011)**. As a result, quantifying these underlying cell
88 fate decisions of how the yeast cells "think" and act in response to external stimuli
89 remains a significant challenge.

90 Indeed, from a microscopic perspective, the cellular decision-making of yeast in
91 response to the mating information is accomplished through the multiple feedback
92 loops **(Figure 2A)**, not only including the positive feedback regulation mediated by
93 Fus3p, but also some negative feedback regulation that can effectively reduce the
94 transcriptional output of this pathway **(Anders et al., 2020; Dohlman et al., 1996;**
95 **Laviña et al., 2010; 2013; Sugiyama et al., 2009; Zheng et al., 2010)**. As known,
96 after pheromone stimulation, there are two pathways that can lead to the polar growth
97 of the cells **(Figure 1)**. The path1 (P_1) is "Fus3p → Far1p/Cdc24p → Cdc42p →
98 Bni1p" **(Butty et al., 1998; Nern and Arkowitz, 1999; 2000b; Shimada *et al.*,**
99 **2000)**. It is realized by entering nucleus through Fus3p to activate Far1, which can
100 escape from the nucleus to activate Bni1p indirectly. The path2 (P_2) is for Fus3p to
101 directly activate Bni1p in the cytoplasm, namely "Fus3p → Bni1p" **(Matheos *et al.*,**

2004). In the process of these two polar growth pathways acting alone or together, the self-activation effect ("Fus3p → Fus3p") of Fus3p caused by pheromones can promote rapid signal transmission (Kranz et al., 1994; Maeder et al., 2007; Serrano et al., 2018; Szczurek et al., 2009). Besides, the activation of the pheromone pathway also induces multiple negative feedback loops, such as "I_1" (Ste5p and Ptp2,3p) (Bhattacharyya et al., 2006; Laviña *et al.*, 2010; 2013; Malleshaiah et al., 2010; Sugiyama *et al.*, 2009; Winters et al., 2005), "I_2" (Sst2p, Msg5p) (Anders *et al.*, 2020; Chen and Kurjan, 1997; Dohlman *et al.*, 1996; Garrison et al., 1999; Laviña *et al.*, 2010; 2013; Parnell et al., 2005; Sugiyama *et al.*, 2009) and "I_3" (Bni1p) (Matheos *et al.*, 2004) in the pathway. It is worth noting that only at high-dose pheromone levels, the negative feedback of the downstream Msg5p will be upregulated (Anders *et al.*, 2020) and only at high concentrations (3μM) of Fus3p, Bni1p will reverse the expression of Fus3p (Matheos *et al.*, 2004).

Here, by observing the multi-dimensional response at the single-cell level, we discovered the non-equilibrium steady states, which demonstrate the cell fates quantitatively, in response to different concentrations of pheromone. These steady states or cellular destinies include two gene expression levels, four growth rates, and four morphological fate states. We quantify these responsive fates of the yeast cells in real time from various dimensions, including the Fus3p gene expression in and out of the nucleus, cell morphology, cell growth rate, and stimulation concentration. Multiple states, as well as switching kinetic rates and pathways among them, are revealed, giving rise to a quantitative landscape of mating response. The applications

of landscape and flux theory to such biological systems enable us to quantify the non-equilibrium dynamics of the yeast cell's mating responses. Our results establish a global and physical framework for understanding cell fate decision-making and mating dynamics. Furthermore, our proposed molecular mechanisms for forming these states, validated by experimental evidence, are the first to quantitatively illustrate the time-dependent evolution of the cell fate decisions. These molecular mechanisms enable the real-time synchronization of intracellular signaling with their physiological growth and morphological functions, bridging microscopic mechanism and macroscopic functions. To further elucidate these microscopic mechanisms, we conduct biochemical reaction simulations to demonstrate the emergence of these states. These findings provide new insights into the global signaling mechanisms underlying how the yeast "think" and do in response to sexual deception.

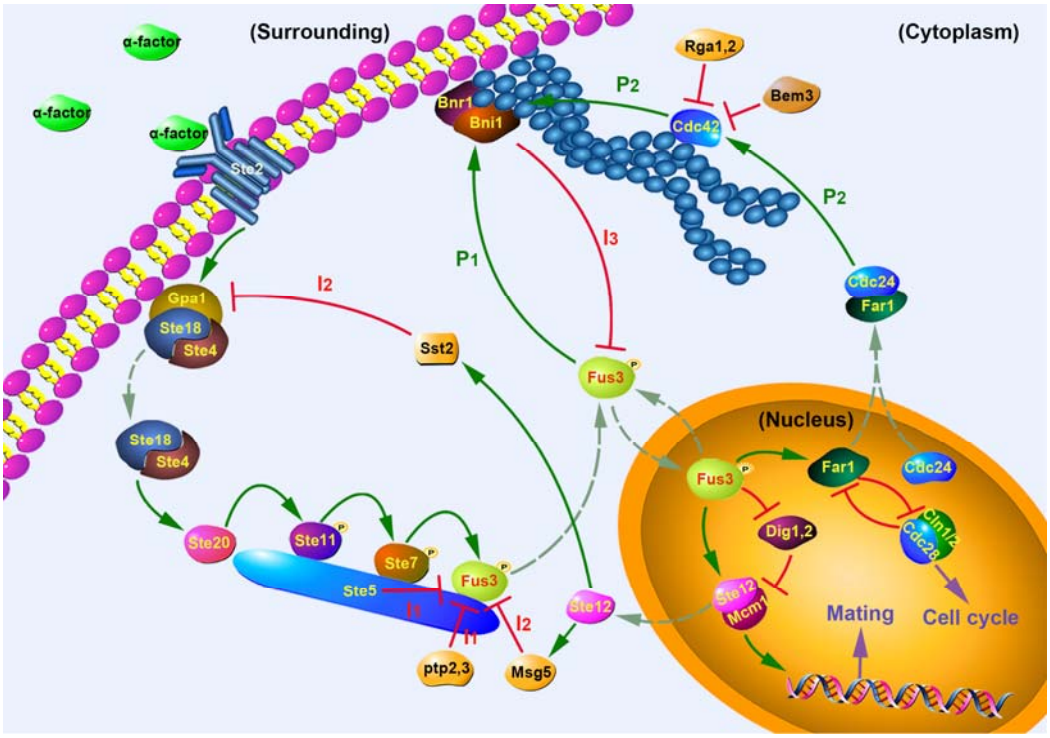

Figure 1. Schematic diagram of mating signal pathway of yeast cell pheromone pathway. The red horizontal line represents the inhibition of negative feedback; the green arrow represents the activation of positive feedback; the light green dashed arrow represents the shift of position; "$I_1 - I_3$" respectively represent different negative feedback adjustment pathways; "P_1" "P_2" represent the two signal pathways of the polar growth.

Results

Quantifying the cellular mating decision

Studies have shown that the yeast, whose mating decision is an all-or-none switch-like response, can automatically filter out the low-dose pheromone signals and only respond near the critical concentration or higher **(Barkai et al., 1998; Doncic et al., 2011; Malleshaiah *et al.*, 2010)**. In fact, the inability of these messengers to attract the attention of the heterosexual yeast is due to the insufficient accumulation of the internal signals, such as Fus3p, which cannot trigger the start of the cell mating preparation project **(Elion et al., 2005; Fiedler et al., 2009; Slaughter et al., 2007)**. Observing the single cell of yeast with a total internal reflection fluorescence microscope, the abundant expression of Fus3p showed that it can gradually reach an "adaptation state" ("a-b" stage) after being stimulated by the pheromone for a certain period of times **(Figure 2B)**. This trend of the rising first and then stabilizing can be understood as the "psychological state" of the yeast cell from being "excited" to restoring the "calm". But if the cells resumed budding ("b-c" stage), the expression of Fus3p was greatly reduced until it returns to near the "initial state" ("0-a" stage).

To gain an initial quantitative understanding of this mating decision in yeast to

159 treat stimuli, the flow cytometry was used to measure the fluorescence intensity of
160 Fus3-GFP in the yeast cells incubated with various pheromone doses for 24 hours.
161 Notably, after 24 hours of cultivation in YPD media containing varying
162 concentrations of the pheromone, the yeast cells in the flow cytometer sample can
163 exist in one of three possible states. The first state occurs when the sample contains
164 only the initial cells ("0-a" stage). This is because the pheromone at low
165 concentrations (0.01-0.4μM) was unable to arrest the cell cycle of the yeast cells from
166 the start. The second state is one in which the solution contains two distinct
167 populations of yeast cells ("a-b" and "b-c" stages). In this state, a moderate
168 concentration (0.4-1.5μM) of the pheromone can arrest the yeast cells' cell cycle from
169 the start, but not continuously for up to 24 hours, causing some yeast cells to resume
170 budding at a later stage. The third state is characterized primarily by the deformed
171 cells ("a-b" stage). Because high concentrations (>1.5μM) of the pheromone can
172 arrest the yeast cells' cell cycle continuously for at least 24 hours. It can be seen from
173 the fitted statistics that the expression of Fus3p at a dose of 0.01-0.4μM shows
174 unimodal distribution of the fluorescence intensities **(Figure 2C)**. The bimodal
175 distribution representing the bistable states gradually begins to appear until the dose is
176 about 0.6μM. This means that the dose of around 0.6μM can begin to attract enough
177 attention from the yeast cells.

178 Using a microfluidic device to cultivate the single-celled yeast in real time under
179 constant temperature conditions, the fluorescence signals and the living state of the
180 yeast cells were recorded with the total internal reflection fluorescent microscope

181 **(Figure 2–videos 1-6 and Appendix 2–legend)**. During the process of culturing with
182 different concentrations of pheromone, we found that the time duration for the yeast
183 cells to inhibit the cell cycle was directly proportional to the concentration of the
184 pheromone. With the prolongation of the pheromone stimulation time, the yeast cells
185 gradually adapt to the external environment and resumed budding reproduction
186 **(Figure 2D)**. This time-sensitive "attitude" towards the messengers shows that there
187 is a certain deadline for the yeast to wait for mating.

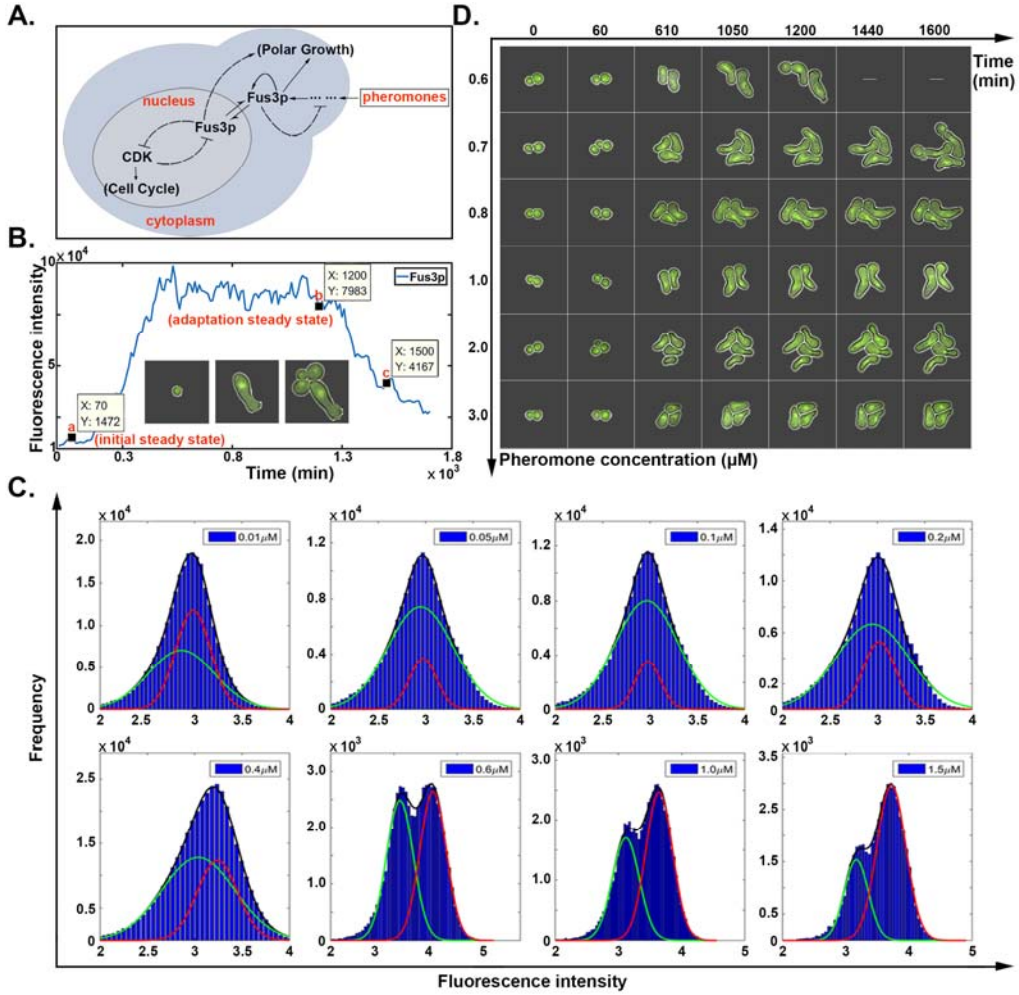

188

189 **Figure 2.** A non-equilibrium biological model for cellular responses. **(A)** Schematic diagram of
190 the signal response dominated by Fus3p in the cell. **(B)** The fluorescence intensity of Fus3p varies

with the pheromone stimulation time at 0.7μM. The x-axis represents the time of incubation with the pheromone-containing medium; the y-axis represents the fluorescence intensity of Fus3p-GFP; the three times “a”, “b” and “c” in the figure show the fluorescence intensity values of pheromone stimulation for 160 minutes, 1520 minutes and 1820 minutes respectively, and the pictures next to them are the single-cell photos of yeast taken through the microscope at that point. **(C)** Statistical graphs of Fus3-GFP fluorescence intensity at different pheromone concentrations. The yeast cells were cultured in YPD medium containing different concentrations of the pheromone for 24h; the black curve represents the overall fluorescence intensity statistics; the green curve represents the “initial steady state” fluorescence intensity; the red curve represents the “adapted steady state” fluorescence intensity. **(D)** Yeast morphology under different pheromone concentrations. The green fluorescence in the cell is the gene expression level of Fus3p; the “60” min in the x-axis represents the time when switching to the pheromone-containing medium for culture. the “610” min represents the time when the cells reach the “adaptive steady state”; the “1050 & 1440” min represent the time points when the cells resume budding reproduction under 0.6μM and 0.7μM pheromone concentrations, respectively.

The online version of this article includes the following source data and video(s) for figure 2:

Source data 1. Data from flow cytometry assays associated with Figure 2C.

Figure 2—videos 1-6. Total internal reflection microscopy images of yeast cell morphology in response to 0.6μM, 0.7μM, 0.8μM, 1.0μM, 2.0μM, and 3.0μM pheromones over time.

Two cell fate decision states reflected on gene expressions

To explore the cell fate decision-making of the yeast during the “calming period” (non-equilibrium steady states), we plotted the fluorescence intensity trajectories of

Fus3p inside and outside the nucleus over time **(Figure 3A and Figure 3–figure supplement 1, 2)**. The trajectories show that Fus3p can reach a stable state when the yeast cells were cultured for about 600 minutes. After removing the data of the unstable process in the previous 600 min, the remaining stationary phase can be quantified by the Fus3p's three-dimensional (in and out of nucleus fluorescence signals) statistical distribution **(Figure 3B and Figure 3–figure supplement 3-5)**. Obviously, there are two steady states, high state (H_1, H_2) and low state (L_1, L_2), of the Fus3p's expressions for both inside and outside the nucleus at the same time. Calculating the "Pearson correlation coefficient" between the intranuclear and extranuclear fluorescence intensities reveals a correlation of approximately 0.8 at various pheromone concentrations **(Appendix 1—table 1)**. This shows a strong linear correlation between the fluorescence intensities of these two positions.

Previous research has demonstrated that the positive feedback regulation induced by pheromones increases Fus3p expression, whereas negative feedback regulation induced by pheromones decreases it **(Anders *et al.*, 2020; Bhattacharyya *et al.*, 2006; Chen and Kurjan, 1997; Dohlman *et al.*, 1996; Garrison *et al.*, 1999; Kranz *et al.*, 1994; Laviña *et al.*, 2010; 2013; Maeder *et al.*, 2007; Malleshaiah *et al.*, 2010; Parnell *et al.*, 2005; Serrano *et al.*, 2018; Sugiyama *et al.*, 2009; Szczurek *et al.*, 2009; Winters *et al.*, 2005)**. However, what the logical connections exist between the pheromone regulatory proteins and these steady-state expression levels of Fus3p? We propose that the tandem of these feedback-regulated logical relationships can serve as a molecular mechanism explaining the emergence of (L_1, L_2) and (H_1, H_2)

235 states. This molecular mechanism is dynamic in nature, involving both functional
236 consumption and feedback loops. First, the functional consumption means that when
237 the amount of the Fus3p in the nucleus is sufficient to inhibit the cell cycle and
238 activate the mating protein ("$\mathrm{Outer\_P_1} \rightarrow \mathrm{Far1p}$ & $\mathrm{Ste12p}$"), the excess Fus3p will be
239 transported out of the nucleus for the polar growth ("$\mathrm{Outer\_P_1} \rightarrow \mathrm{Inner\_P_1}$" and
240 "$\mathrm{Inner\_P_2} \rightarrow \mathrm{Outer\_P_2}$") **(Figure 3C)**; Second, the feedback loop implies that Fus3p
241 regulates its own expression by activating or inhibiting it. For example, the feedback
242 loop "A → Fus3p ┤A" is primarily concerned with the pathway involving Gpa1p and
243 Sst2p, while the feedback loop "Fus3p → B ┤Fus3p" is primarily concerned with the
244 pathway involving Ste12p and Msg5p **(Figures 1 and 3D)**.

245 If our dynamic molecular mechanism is correct, functional consumption and
246 feedback loops undoubtedly cause Fus3p's expression to alternate between high and
247 low levels. Besides, the polar growth should mainly appear in the high state (H_1, H_2),
248 and essentially no significant growth would occur in the low state (L_1, L_2). To
249 validate this dynamic molecular mechanism, we fitted the single-track fluorescence
250 intensity during the "adaptation steady state" period. Clearly, the two trajectory fates
251 (high state & low state) inside and outside the nucleus can be switched between the
252 corresponding two fates respectively **(Figure 3E)**, confirming our logical
253 interpretation of the state switching above.

254 Biologically, this switching of the two fates shows the yeast's two decision-
255 makings, looking for a mate or waiting for a mate. Immersed in the low state (L_1, L_2)
256 does not directly restore budding but chooses to continue intermittent growth, which

means that the yeast cell doesn't give up mating even if its spouse missed their appointment. On the other hand, the yeast is also actively saving itself, accumulating the counter-attack power through many negative feedback regulators, to escape the deception of lies. This cellular behavior that not only waits hopefully, but also actively strengthens its resistance to prevent disappointment, which seems to be paradoxical. In fact, it shows that the yeast is not "losing its mind" as a result of being deceived, but rather is making the "sane" decisions.

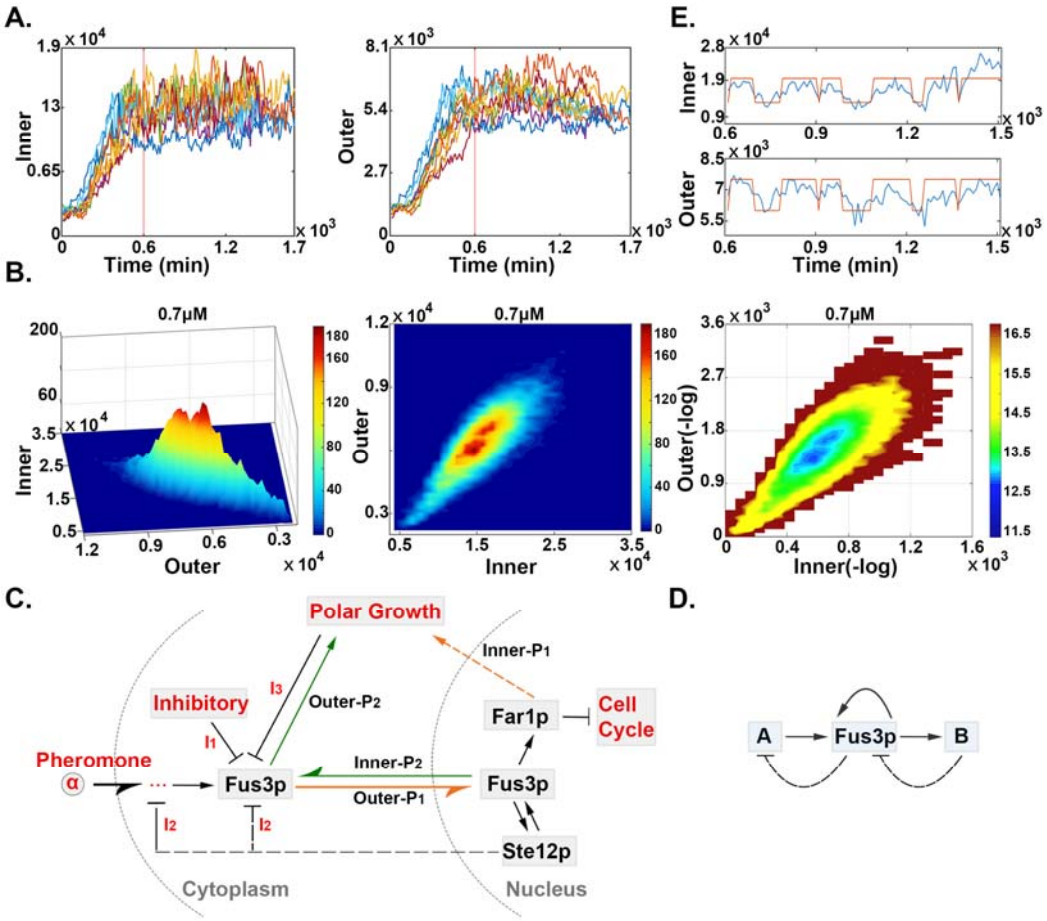

Figure 3. The two steady states of the gene expressions. **(A)** The fluorescence intensity trajectories of Fus3p inside and outside the nucleus over time at 0.7μM. The red vertical line is the

267 dividing line of time, and the 600 minutes is also the starting point of steady-state data; **(B)** Three-
268 dimensional distribution graph of Fus3p fluorescence intensity inside and outside the nucleus of
269 yeast cells in the stationary phase under the different pheromone concentrations. On the left is the
270 3D distribution of fluorescence or the 3D population landscape, on the middle is the 2D
271 histograms or the 2D underlying potential landscapes U in exponential scale (defined as $p \sim e^{-U}$),
272 which is also the population landscape; on the right is the 2D underlying potential landscapes U
273 ($U = -\ln P$). **(C)** Schematic diagram of the response of yeast cells to pheromone stimulation. The
274 solid line is the path that plays a major role in the polar growth, and the dashed line has a smaller
275 weight on the polar growth than the solid line; the "$\mathrm{Outer\_P_1}$" represents the indirect pathway of
276 the Fus3p in the cytoplasm to the nucleus for inhibiting the cell cycle; the "$\mathrm{Inner\_P_1}$" represents
277 the indirect pathway for the Fus3p in the nucleus for the cell polar growth; the "$\mathrm{Outer\_P_2}$"
278 represents the direct pathway of the Fus3p in the cytoplasm for the cell polar growth; the
279 "$\mathrm{Inner\_P_2}$" represents the direct pathway for the Fus3p in the nucleus to transfer to the cytoplasm
280 for the cell polar growth; the "$I_1 - I_3$" represent the inhibitory effects of the negative feedback
281 regulation; the two gray dashed lines represent the cell membrane and the nuclear membrane,
282 respectively. **(D)** A simplified schematic diagram of the molecular mechanism of Fus3p's self-
283 activation and self-inhibition. A and B respectively represent two genes that interact with Fus3p in
284 the signaling pathway; the solid line represents self-activation; the dashed line represents self-
285 inhibition. **(E)** The fluorescence intensity trajectories of Fus3p inside and outside the nucleus over
286 time. The red line represents the fitting line of the high state and the low state.
287 The online version of this article includes the following source data and figure supplement(s) for
288 figure 3:

Source data 1. Data required to create the landscape for Figure 3B.

Figure supplement 1-2. Fluorescence intensity trajectories of intranuclear and extranuclear Fus3p in response to varying concentrations of pheromone.

Figure supplement 3-5. Potential landscapes U of intranuclear and extranuclear Fus3p in response to varying concentrations of pheromone.

Figure supplement 6. The distribution graph of the fluorescence intensity of all pixels in the cell with time.

Uncovering the decision landscapes in the pheromone dimension

To further understand the nature of the bistable state, we counted the apparent characteristics of the double peaks, such as the area overlap ratio (w) and the spacing between the double peaks **(Figure 4A)**. From the calculation results, we can see that as the pheromone concentration increases, the area overlap ratio (w) between the two states first increases (0.7μM-1.0μM) and then decreases (2.0μM-3.0μM), while the bimodal distance first decreases and then increases. As the peak distance decreases, the area overlap ratio of the double peaks increases, reflecting the gradual closeness of the two gene expression states.

To uncover the capability of the switching between these two decisions, the hidden Markov chain model (HMM) is used to fit the experimental data perform the bi-stable analysis on the decision-making landscape. The steady state probability can be used to quantify the population landscape P or the potential landscape U **(Fang et al., 2019; Feng et al., 2014; Wang, 2015; Wang *et al.*, 2008a)**, where U is defined as the negative logarithm of the steady state distribution P of the gene expressions,

311 $U = -\ln P$. As seen clearly, the population and potential landscapes (P and U) at
312 various pheromone concentrations have two basins of attractions and they are
313 separated by the barriers in between **(Figure 3B and Figure 3–figure supplement 3-**
314 **5)**. The barrier height can be directly obtained from the landscape, while the transition
315 rates and the residence times of the states were all calculated quantitatively from the
316 HMM model fitting to experimental data **(Figures 4B and C)**.

317 According to the results, the trend of the barrier height versus pheromone
318 concentration is essentially consistent with that of its residence time (**Figure 4B**). The
319 greater the barrier height in the decision-making is, the greater the resistance to
320 switching is. A slight increase in barrier height significantly increases the residence
321 time of the "high-state" for polar growth at low doses (0.7-0.8μM). At the high doses
322 (1.0-3.0μM), the residence time also decreases gradually as the barrier height
323 decreases. From a biological perspective, this increase at low doses is due to the
324 positive feedback regulation ("Pheromone → Fus3p" & "Fus3p → Fus3p") in the
325 gene network, whereas the decrease at high doses is owing to a stronger negative
326 feedback regulation (such as "I_3") **(Figures 1 and 3C)**. Meanwhile, the opposite trend
327 of the transfer rate ratio (k_{21}/k_{12}) to the barrier height ratio or the residence time ratio
328 (High/Low) upon the pheromone concentration changes reflects the weighting of
329 these two decisions to switch (**Figure 4C**). A higher weight for the "high-state"
330 indicates fewer transitions from high to low state per unit time, and more time for the
331 yeast to perform polar growth. To understand this relationship more clearly, the
332 potential landscape topographies are shown under different pheromone doses **(Figure**

4D). Due to the relatively greater resistance to the switching from the high-state to the low-state at the low doses, the yeast is more inclined to stay in the high state to look for mating actively, while the opposite is true at the high doses.

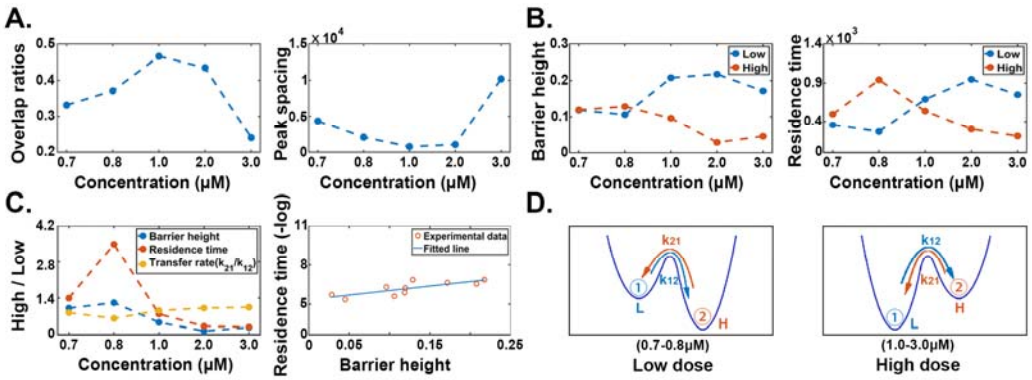

Figure 4. The decision landscapes in the pheromone dimension. **(A)** The apparent characteristics of the double peaks in the fluorescence distribution under the changes in pheromone concentration. The "w" is the area overlap ratio between the double peaks; the peak spacing is the distance between the main axes of the high state and low states of the bimodal distribution. **(B)** The statistical trends of the barrier height and residence time with the changes in pheromone concentration. **(C)** Relationships between various characteristics for the potential landscape with the changes in pheromone concentration. the "k_{12}" is the transition rate from low state to high state; the "k_{21}" is the transition rate from high state to low state; The red circles are the data points, the blue line is the fitted line of the data, the correlation coefficient of the barrier height and the residence time is 0.79 (Significantly positive correlation). **(D)** Simple schematic diagram of the potential landscape topography under different pheromone dosages. "L & ①" stands for the low state, "H & ②" stands for the high state; the "k_{12}&k_{21}" are the transition rates between the low state and the high state.

350 The online version of this article includes the following source data for figure 4:

351 **Source data 1.** Data tables related to quantifications in Figure 4A.

352 **Source data 2.** Data tables related to quantifications in Figures 4B and C.

353 **Four spatiotemporal cell growth rate states**

354 Using real-time microscopy observations, we discovered that the cell growth rate
355 of yeast was not uniform across time periods. Except for the top, other parts of the cell
356 changed slightly as the yeast stretched forward. To accurately measure the
357 spatiotemporal change rate of the cell morphology, we used the circular filling pattern
358 to segment yeast cells **(Figure 5A)**. It is obvious that the largest circle represents the
359 initial main part of the cell, while the smallest circle represents the newly formed
360 portion at the cell's top. For example, inside the yeast cell, there are two filled circles
361 denoted by the letters R_0 and R_1. R_0 is the larger circle, while R_1 is the smaller one
362 **(Figure 5B)**. If the filled circle R_1 of the cells grows uniformly in size from small to
363 large (Model-1: "$R_{1\_1} \rightarrow R_{1\_2} \rightarrow R_{1\_3} \rightarrow R_{1\_4}$"), then the ratios of the smallest circle to
364 the largest circle in the cell will be uniformly distributed. If, on the other hand, the
365 cell grows in model-2 ("$R_{1\_1} \rightarrow R_{1\_2} \rightarrow R_{1\_3} \rightarrow R_{1\_3} \rightarrow R_{1\_4}$") with the growth
366 temporarily halted at R_{1_3}, the R_{1_3} will be observed repeatedly, increasing the
367 probability of the R_{1_3}/R_0. When the size ratio of the smallest and largest circles was
368 used as an observable value, we noticed that the statistical result was mostly around
369 0.27 at 0.7μM **(Figure 5C and Figure 5–figure supplement 1)**. This demonstrates
370 unequivocally that when the size ratio is 0.27, cellular growth is slower, allowing for
371 more opportunities to observe this ratio distribution. That is, the rate of growth or the

capacity for growth at various locations within the cell are not exactly identical. Therefore, rather than using the cell's area, the total length, or the arithmetic mean of the length, we chose to describe the cell's morphology using the reciprocal of the radius in the cell-filled circle multiplied by the number of filled circles, i.e. $H_n = n(\frac{1}{R_1} + \frac{1}{R_2} + \ldots + \frac{1}{R_n})$. The rate of change in the cell morphology is denoted by $(\left|\frac{H_{n+1} - H_n}{2}\right| - \left|\frac{H_n - H_{n-1}}{2}\right|)/(t_{n+1} - t_n)$.

From the real-time trajectory of the changes in the cell morphology, measured by the H_n of the cell filled circles, we found that there were roughly four types of the cell shape changes. According to the definition of H_n describing the cell morphology, we know that the ascending phase of the curve $(t_1 - t_2)$ mainly represents the change of the cell length, while the descending phase $(t_3 - t_4)$ mainly denotes the change of cell width, and the slight change phase $(t_2 - t_3)$ & $(t_4 - t_5)$ characterizes that the cells almost stop growing or grow at a low speed **(Figure 5D)**. The Supplementary Section discusses this justification for the cellular morphological characterization. We collected the statistics on the distribution of the cell growth rate **(Figure 5E and Figure 5–figure supplement 2)**. It is obvious that the cell growth rate can be divided into four states if the positive and negative values are distinguished. We divided these four growth rates into two categories: the fast growth rates and the slow growth rates. The fast growth rates included the length-first rate one (representing the longitudinal growth rate) and the width-first rate one (representing the lateral growth rate); the slow growth rates included two non-obvious rates (representing the slightly length-first & width-first growth rates).

To explore the cellular decisions behind these four growth rates, the response speed of the proteins in the signal transduction pathway is considered to determine the formation of the four behaviors (the supplementary section discussed this issue of protein response speed in greater detail). Many studies have shown that Fus3p and Far1p were both important genes for the formation of the cell growth axis determined by the bud site and the mutants. Lacking of Far1p or Fus3p would cause the mis-localization of the shmoo projections **(Butty *et al.*, 1998; Nern and Arkowitz, 1999; 2000a)**. Therefore, we suggest that "P_1" is more directional than the "P_2" (longitudinal growth). In summary, we propose that the molecular mechanism of the length-first rate is mainly described by the graph "P_2", the width-first rate is mainly illustrated by the graph "$P_1 + P_2$", and the non-obvious rates are mainly shown by the graphs "P_0" & "P_1" **(Figure 5F)**. Meanwhile, the experimental evidences of these four molecular mechanisms have been indirectly confirmed in the following self-consistent analysis.

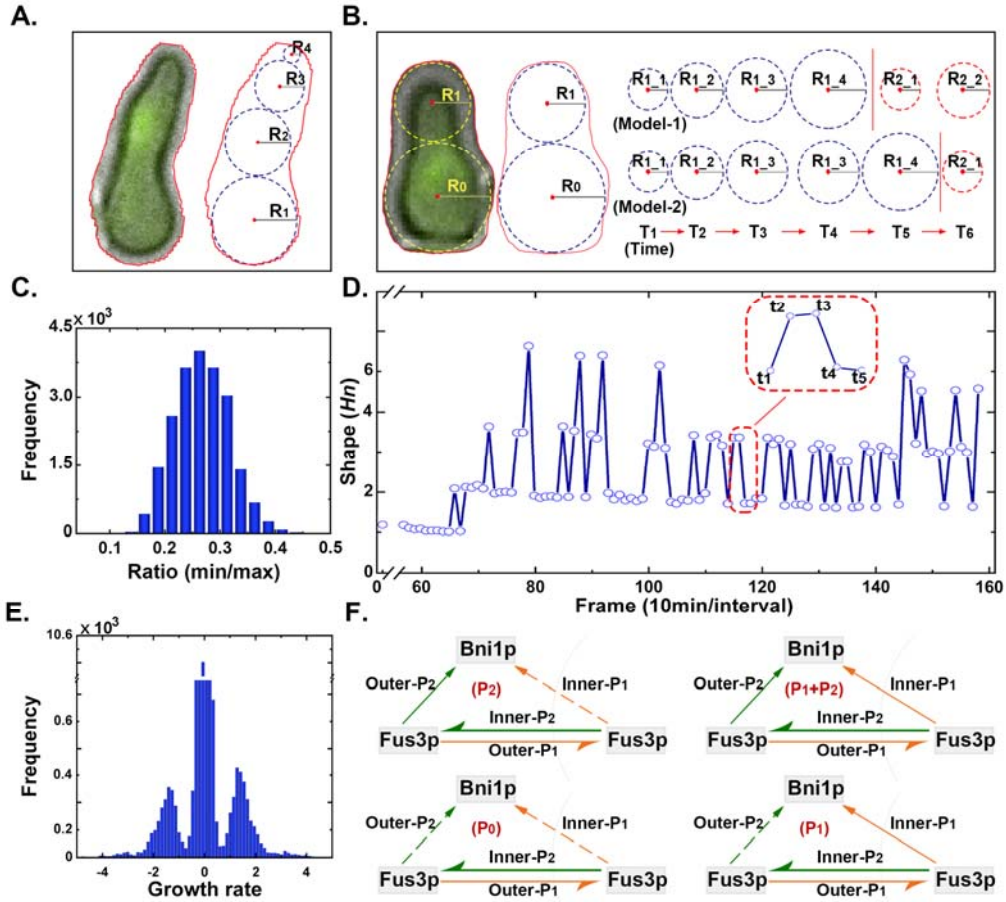

Figure 5. The underlying molecular mechanism of the cell growth rate. **(A)** Simple diagram of cell shape with circle filling pattern. The left picture shows one yeast cell cultured for 1020 minutes in a medium containing 0.7μM pheromone; the red line is the boundary line of the cell shape; the right picture is the filling model of the left picture; the "$R_1 - R_4$" are the radii of the circle. **(B)** The illustration of the scheme for simulated cell growth. The R_0 is the maximum circle radius; the R_1 is the minimum circle radius; the $(R_{1\_1}), \ldots, (R_{1\_4})$ are the radius of the R_1 in the different growth stages; the $(T_1, \ldots, T_6)$are the times; **(C)** The distribution diagram of the radius ratio between the smallest circle and the largest circle of the yeast cell shape at 0.7μM. **(D)** Real-time trajectory of the cell morphology (H_n) at 0.7μM. **(E)** The distribution statistics of the cell growth rate at 0.7μM. **(F)** Schematic diagram of the four molecular mechanisms of the polar

growth of yeast cells. Figure 2C includes the same additional annotations.

The online version of this article includes the following source data and figure supplement(s) for figure 5:

Source data 1. The ratio data of the smallest filled circle to the largest filled circle in Figure 5C.

Source data 2. Cell growth rate statistics associated with Figure 5E.

Figure supplement 1. The distribution diagram of the radius ratio between the smallest circle and the largest circle of the yeast cell shape under the different pheromone doses.

Figure supplement 2. Statistical graph of the cell growth rate under the different pheromone doses.

Experimental evidence for the molecular mechanisms

To validate the above-mentioned molecular mechanism, we investigated the link between the growth rates and dual fluorescence gene expression states. By taking the absolute value of the growth rate, we directly divided into the "Fast growth rate" and the "Slow growth rate" states **(Figure 6A and Figure 6–figure supplement 1)**. Then, we gathered the Fus3p fluorescence intensity data inside and outside the nucleus and plotted a two-dimensional statistical distribution against the growth rate data separately **(Figure 6B and Figure 6–figure supplement 2, 3)**. In principle, the "High-state" fluorescence data should be completely included in the "Fast-state" growth rate data, and the "Low-state" fluorescence data should also be completely included in the "Slow-state" growth rate data. However, the behavior we have observed is obviously not the case. When using the different colors to represent the fluorescence states, we can clearly see that the low state (red dots), high state (blue

441 dots), and the overlapping data (green dots) are all included in the two growth rates.
442 The biological meaning of these overlapping data is the fast growth of the yeast in a
443 low-fluorescence state ("*FL*") and the slow growth of the yeast in a high-fluorescence
444 state ("*SH*").

445 For the dynamical understanding of the cellular decision-making, the mate-
446 seeking behavior of the yeast cells through the polar growth occurs primarily when
447 the Fus3p is in the high fluorescent state. To explore the rationality of the existence of
448 this mixing behavior, we compared the similarity of the real-time trajectories between
449 Fus3p fluorescence intensity and cell growth rate. The similarity of these two types of
450 trajectories indicates that the overlaps are not very big **(Appendix 1—table 2)**. The
451 "Fast state" is mostly contained in the "High state", and the "Slow state" is mostly
452 contained in the "Low state" **(Appendix 1—table 3)**. This indicates that Fus3p's
453 regulation and the cell growth rate are not completely independent and uncorrelated
454 events. We suggest that these mixed states ("*FL & SH*") emerge as a result of certain
455 overlap between the fluorescent double states (See the appendix text for a more
456 detailed discussion). When distinguishing the fluorescence intensity state of the
457 overlapping area, the fluorescence intensity indicated that the large fluorescence
458 intensity had certain probability of belonging to the "Low-state", on the contrary, the
459 small fluorescence intensity also had certain probability of belonging to the "High-
460 state" **(Figure 6C)**. Therefore, the "*FL*" represents the state of "Fast" growth rate and
461 "Large-intensity" in the "Low-state" fluorescence; the "*SH*" represents the state of
462 "Slow" growth rate and "Small-intensity" in the "High-state" fluorescence.

To better describe the overlapping effect of the fluorescence data, we create a schematic diagram that illustrates the mixed area of fluorescence intensity **(Figure 6D).** Among them, the "γ_{FL}", "γ_{SH}", "γ_{FH}" and "γ_{SL}" respectively represent the proportion of the state of "*FL*", "*SH*", "*FH*" and "*SL*" in the growth rate data; the "N_f" and "N_s" is the number of the "Fast-state" growth rate data and the "Slow-state" growth rate data respectively. Subsequently, we calculate the overlap ratio distribution and the weights of the four states in the total fluorescence data at different concentrations of pheromone **(Appendix 1—table 4)**. The overlap rate being equal to the ratio of the "*FL*" and "*SH*" states to the total data ($w' = (\gamma_{FL} \cdot N_f + \gamma_{SH} \cdot N_s)/(N_f + N_s)$) is basically the same as the overlap area of the high and low fluorescence states (w'). This provides indirect experimental evidence to support this quantitative understanding of the molecular mechanism underlying cell fate decision-making.

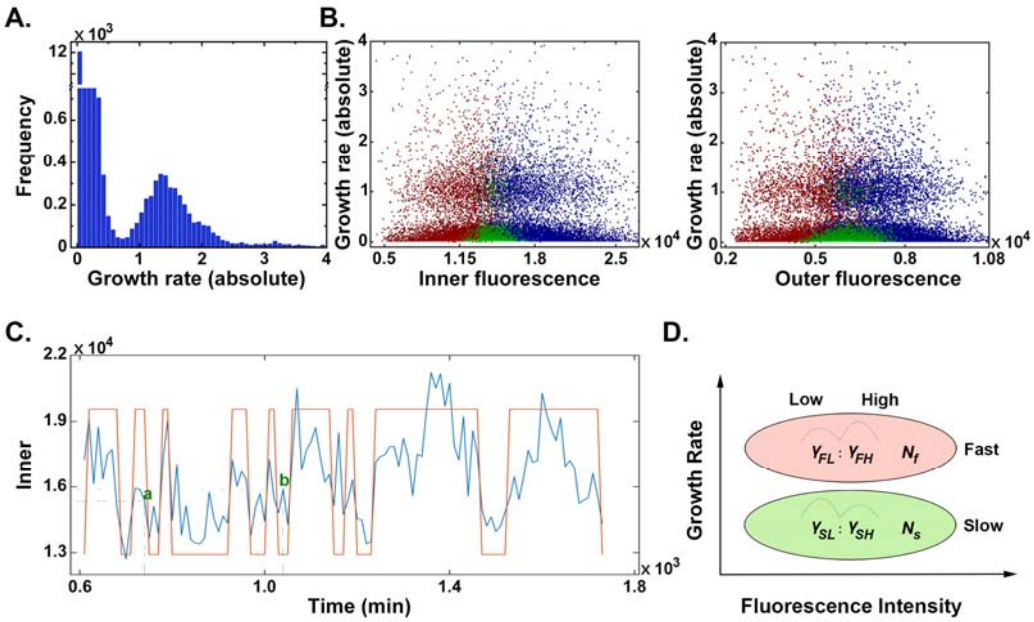

Figure 6. The relationship between the growth rate and the bistable gene expressions. **(A)** Statistical graph of the distribution statistics of the absolute value of the cell growth rate at 0.7μM. **(B)** Two-dimensional statistical distribution of fluorescence data and growth data inside and outside the nucleus at 0.7μM. The red dots represent the low fluorescence state, the blue dots represent the high fluorescence state, and the green dots represent the mixed state. **(C)** The trajectory graph of the fluorescence intensity of Fus3p in the nucleus over time. The blue curve is the fluorescence trajectory; the red line is the curve of the state with time after the fluorescence intensity is fitted, the upper one is the "High-state", the lower one is the "Low-state"; "a" and "b" are the two points in the "High-state" and the "Low-state" fluorescence intensity, respectively. **(D)** Diagram depicting the relationship between data of various dimensions. The "$\gamma_{FL}:\gamma_{FH}$" represents the ratio of the "Low-state" to the "High-state" of the fluorescence intensity in the "Fast-state" growth rate data; the "$\gamma_{SL}:\gamma_{SH}$" represents the ratio of the "Low-state" to the "High-state" of the fluorescence intensity in the "Slow-state" growth rate data; "N_f" is the number of the "Fast-state" growth rate data; the "N_s" is the number of the "Slow-state" growth rate data.

The online version of this article includes the following source data and figure supplement(s) for figure 6:

Source data 1. Statistics of the absolute growth rates of cells associated with Figure 6A.

Source data 2. The cell growth rate and fluorescence intensity data presented in Figure 6B.

Figure supplement 1. Statistical graph depicting the absolute value of the cell growth rate at various pheromone concentrations.

Figure supplement 2-3. Statistical diagram depicting the relationship between the fluorescence intensity of Fus3p inside and outside the nucleus and the cell growth rate at different pheromone

concentrations.

Figure supplement 4. A simplified diagram of the overlap effect of the dual-state fluorescence data.

Four cell morphological fate states

When the cell morphology data were analyzed using the H_n, the cell shape revealed the presence of four distinct fates ("$F_1 - F_4$") in response to varying pheromone stimulation doses **(Figure 7A and Figure 7–figure supplement 1)**. From the photos of these fates taken by the microscope, it can be seen that their aspect ratios are obviously inconsistent **(Figure 7B)**. Although we already know the four molecular mechanisms that lead to different cell growth rates, are these different molecular mechanisms the direct cause of the fates of the four cell morphologies? Indeed, the cell morphology is a cumulative quantity distinct from the cell growth rate, the formation of which is dependent on the growth of cell in a variety of directions. Therefore, we propose that the cell morphology cannot be determined solely by the action of a single growth pathway, such as "$P_1 + P_2$", "P_2", "P_1", "P_0" **(Figure 5F)**, but should be the result of their combined action.

To understand the molecular mechanisms of the four cell morphological fates more intuitively, we used the growth ability represented by the growth rate of the cells in different directions to count the synergistic effect of the minor axis and major axis of the cell **(Figure 7C)**. From the Figure, we can see that there are four distinct states in the cooperative distribution of the two data, which strongly suggests that the ability to grow from different directions is a key determinant forming the cell morphology.

Importantly, it is entirely due to the four combinations of these two growth abilities that make the cells to form four stable morphological fates. These two growth abilities show the comprehensive considerations of the yeast in the decision-making process.

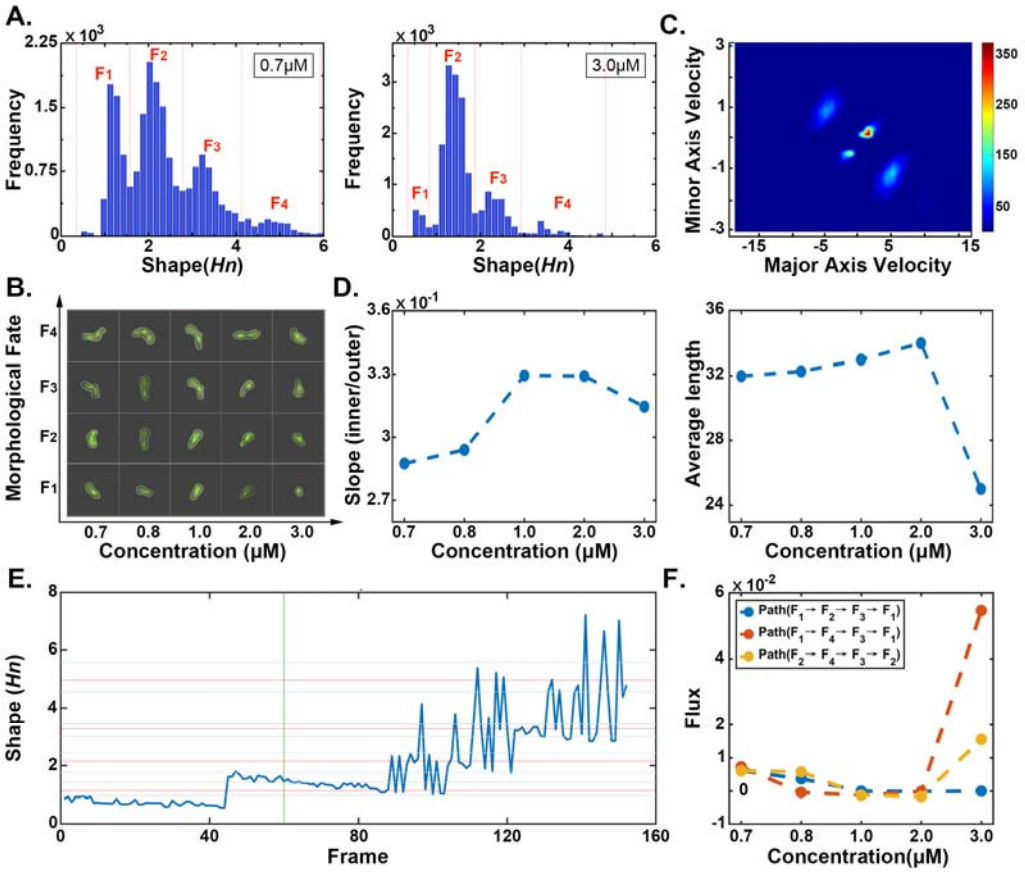

Figure 7. The understanding of the different cell morphological fates. **(A)** Statistical distribution of cell morphology at 0.7μM. The red vertical lines are the dividing lines of different cell morphologies; the "$F_1 - F_4$" represent the four cell morphological fates respectively. **(B)** Photographs taken by fluorescence microscope of cells with four cell morphological fates under different pheromone concentrations. **(C)** The statistical distribution of the growth rate of the cells in different directions at the pheromone concentration of 0.7μM. The ordinate represents the growth rate of the minor axis of the cell, and the cell width is represented by the average radius of

533 the filled circle; the abscissa represents the growth rate of the major axis of the cell, and the cell
534 length is represented by the sum of the diameter of the filled circle. **(D)** Trend statistics of the
535 nuclear to cytoplasmic fluorescence ratio (slope) and the average cell length changing with the
536 pheromone concentration. **(E)** A single trajectory diagram of cell morphology over time at the
537 pheromone concentration of 0.7μM. The abscissa is the number of frames taken by the
538 microscope, one frame is taken every 10 minutes; the green vertical line is the dividing line of the
539 steady-state data; the red line is the center line of the four cell shapes ($F_1 - F_4$); the light lines on
540 both sides of the red line are the two boundary lines of the four cell shapes ($F_1 - F_4$); **(F)** The net
541 flux of the conversion between the four cell morphologies at different concentrations of
542 pheromone.

543 The online version of this article includes the following source data and figure supplement(s) for
544 figure 7:

545 **Source data 1.** Cell morphology data associated with Figure 7A

546 **Source data 2.** Data tables related to quantifications in Figure 7D.

547 **Source data 3-7.** Data generated during calculations of the net flux associated with Figure 7F.

548 **Figure supplement 1.** The Statistical distribution of the cell morphological fates under the
549 different pheromone doses.

550 **Figure supplement 2.** The slope of the Fus3 fluorescence intensity distribution under the different
551 pheromone doses.

552 Biological puzzle solved by landscape and flux theory

553 By quantifying the average cell length and the nuclear-to-cytoplasmic ratio, it
554 can be concluded that the high-dose pheromone concentrations (3.0μM) break the

linear monotonic trend at the low doses (0.7μM-2.0μM) **(Figure 7D and Figure 7–figure supplement 2)**. We suggest this biological puzzle is caused by the yeast awakening from being deceived. On a macroscopic level, the yeast cells begin to spend more time waiting for mating rather than actively looking for mating, which has been proved by the residence time of the high-state and the low-state in the decision-making landscape. On a microscopic level, this awakening at high doses is characterized by an increased capacity for negative feedback regulation (such as "I_3") to inhibit the second polar growth pathway ("P_2") **(Figures 1 and 3C)**. Three-quarters of the cell fates (except F_2) showed a sudden reduction in morphology at high dose (3μM), likely attributing to this impaired "P_2" function **(Figure 7A and Figure 7–figure supplement 1)**. This impairment undoubtedly leads to a reduced combination of the lateral and vertical cell growth patterns, as well as a more unstable landscape containing four morphological fates at 3μM dose than those at other lower doses.

To verify the instability in the cellular morphological landscape caused by this awakening, we compared the single trajectory of the different cell morphologies over time. We found that there were twelve combinations of switching between any two different shapes **(Figure 7E)**. The twelve combinations of the switching mean that the four shapes (H_n) can be converted among each other, which is also possible to bring about a net surplus transition probability. Using the hidden Markov chain model to fit the experimental data perform statistical analysis, the transition probability between the different cell morphologies does show three kinds of net fluxes **(Figure 7F)**, which provide an important indicator of the non-equilibrium steady-state **(Wang,**

577 **2015; Wang *et al.*, 2010a; Wang *et al.*, 2008a)**. Interestingly, the intensities of the
578 three net fluxes decrease first and then increase with the increase of the pheromone
579 concentrations, showing a specific monotonous trend in the opposite direction similar
580 to the average length of the cell. The larger the net flux is, the more unstable the cell
581 morphology landscape becomes, which confirms that the yeast has begun to wake up
582 from being deceived by the high dose (3μM).

583 **Simulations for the signal transduction and the cell growth**

584 According to the functional and quantitative regulation obtained from the
585 database, such as KEGG, EVEX etc., we established a simplified signal transduction
586 model from the perspective of the global gene regulatory networks **(Figures 1, 8A**
587 **and B)**. This model consists of a set of biochemical reactions simulated using the
588 Gillespie algorithm **(De Jong, 2002; Gillespie, 2000; 2001)** **(Appendix 1—table 5-**
589 **7)**. Through the statistics of the chemical reaction results in the simulation, the
590 fluorescence distribution of Fus3p inside and outside the nucleus showed a two-state
591 behavior, confirming the rationality of the emergence of the bimodal fluorescence
592 state in the molecular mechanism **(Figure 8C)**.

593 Meanwhile, the dynamical process of the cell growth is simulated using the
594 Bni1p generated in the reactions. Although both the growth pathways ("P_1", "P_2") are
595 involved in the growth process of the cellular length and width, the weights of the
596 pathways that grow in the two directions are significantly different. Therefore, we
597 directly define the "Bni1_in" produced by the "P_1" that plays a major role as the
598 growth of the major axis, and the "Bni1_out" produced by the "P_2" as the growth of

the minor axis.

In this simulation, the a denotes the radial length of the yeast cell, while the "b" denotes the transverse length of the yeast cell **(Figure 8A)**. Each iteration increases the radial and transverse lengths of the yeast cell by "δa" and "δb", respectively. "δa" is proportional to "PBni1p_in" and inversely proportional to "b", meanwhile, "δb" is proportional to "PBni1p_out" and inversely proportional to "a". That is $\delta a = \frac{r_a(P\text{Bni1p\_in})}{b}$, $\delta b = \frac{r_b(P\text{Bni1p\_out})}{a}$. It is shown that the value "N" is the rounding operation of $\frac{a}{b}$, i.e. $\left[\frac{a}{b}\right]$, and "c" is the residual amount after rounding **(Figure 8B)**. The H_n is $(N+1)(N/b+1/c)$. The distribution of the cell morphology shows four fates, which are the same as the experimental results **(Figure 8D)**.

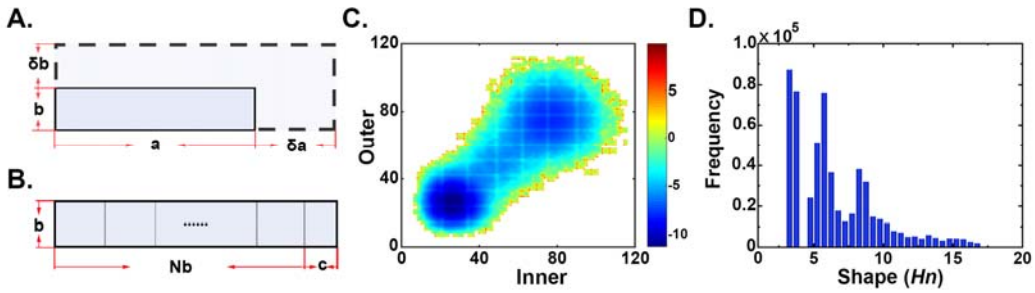

Figure 8. Simulations for the signal transduction and the cell growth. **(A)** The scheme of simulated cell growth. "a" represents the length of the cell; "δa" is the increased length of the cell, "b" represents the width of the cell; "δb" is the increased width of the cell. **(B)** The scheme of the "H_n" calculation. "c" means the remainder of cell length divided by "b"; "N" represents the number of "b". **(C)** Distribution graph of the negative log of the number of Fus3p fluorescence intensity inside and outside the nucleus of yeast cells in the stationary phase using simulation. **(D)** The distribution of the cell morphology (H_n) using simulation.

The online version of this article includes the following source data for figure 8:

618 **Source data 1.** The outcomes of simulation calculations associated with Figures 8B and C.

619

620 ## Discussion

621 In this study, we used the biological and physical tools to quantitatively uncover
622 and understand the cell fate decision-making of the yeast after encountering sexual
623 deception. To understand the "psychological process" of its internal activities, a total
624 internal reflection microscope and a microfluidic system were used to observe the
625 gene expression levels of the Fus3p inside and outside the nucleus of the yeast in real
626 time. The "attitude" towards the incoming messengers under the different doses of
627 pheromone can be observed from the fluorescence intensity trajectories of the Fus3p.
628 The ascending phase of the Fus3p's curve is the "excitement period" to adapt to the
629 external stimuli, while the steady phase of the curve shows the "calming period" of
630 the yeast cell. Due to the "calming period" (adaptation steady period) of the yeast
631 during the "adaptation period" under the 0.6μM pheromone being relatively short, we
632 selected five concentrations that can capture "enough attentions" by the yeast as the
633 external stimulus conditions.

634 If the yeast, like other higher organisms, becomes "angry" after encountering
635 sexual deception, is its subsequent polar growth an irrational behavior? Some studies
636 believe that the establishment of polarity helps organisms to survive better in nature
637 **(Dworkin, 2009; Treuner-Lange and Sogaard-Andersen, 2014)**. Since the
638 chemotactic reactions used by yeast for mating cannot move as the E. coli, its polar
639 growth can only grow towards the high concentrations of pheromone for achieving

640 the mutual contact and fusion finally **(Bardwell, 2004; Macnab and Koshland,**
641 **1972; Sourjik and Wingreen, 2012)**. Considering the "attitude" of the yeast cell in
642 the "excitement period", it seems that the description of the polar growth as searching
643 for a mate is a rational behavior at this time. However, how to understand the
644 "psychological state" of the polar growth after the yeast has restored to the "calm"?
645 We found that the cellular decision-making landscape was presented during the
646 "calming time". When the Fus3p is in the low state (L_1, L_2), the yeast cell will stay in
647 place to wait for mating. In the high state (H_1, H_2), the yeast cell will actively grow in
648 polarity to look for its mate. This switching between the waiting for mating and
649 looking for mating indicates that the decision-making of the yeast cell is "sane" rather
650 than impulsive behavior after being "angry".

651 When the yeast is determined to switch its decision from one to another, how
652 strong is the resistance to switch, how fast is the conversion and how long is the
653 waiting time for each behavior? To understand these problems that the yeast needs to
654 face, we further quantitatively explored the barrier height, switching rate and the
655 residence time in the decision-making landscape of the yeast at different doses
656 **(Figures 4B and C)**. Comparing the various shapes of the landscapes, the intuition
657 that the greater the barrier height characterizing the potential landscape topography is,
658 the longer the residence time of the state is **(Fang *et al.*, 2019; Wang *et al.*, 2011)**, can
659 be fully confirmed by our experimental data.

660 In the process of the polar growth, which direction should be grown and how fast
661 it should be growing are questions that the cell has to think about. To explore this

662 cellular decision-making of the yeast when looking for its mate, the growth direction
663 is divided into the longitudinal growth and the lateral growth, and the growth rate is
664 divided into the fast-speed growth and the low-speed growth. We suggest that the
665 underlying molecular mechanism of these decisions is due to the different response
666 speeds of Fus3p to the signals. Although the current technology cannot distinguish the
667 individual work done by each Fus3p molecule in the cell, we can reveal a global
668 understanding of the underlying rules based on the expressions of all the Fus3p. Thus,
669 the experimental evidences of the molecular mechanism that leads to the growth rate
670 can be confirmed from the self-consistent relationship between the fluorescence data
671 and the growth rate data.

672 Considering that the spouse may be in the different positions, does the yeast have
673 a variety of deformed plans to achieve fusion? When encountering the deformed
674 forms in the polar growth, the yeast showed four morphological fates, which were
675 caused by the combined action of the cellular decision-making in the two directions as
676 we have proved. Obviously, these four decision-making results undoubtedly increase
677 the diversity of the yeast mating fates and reduce the probability of the cell failing to
678 look for its mate in the end.

679 Meanwhile, the net fluxes generated by the mutual conversions between the
680 morphological fates also provide us with an opportunity to confirm the "psychological
681 activity" of the yeast. According to our study, the greater the net flux leads to the
682 greater the spiral force in the non-equilibrium steady state **(Li et al., 2011; Wang,**
683 **2015)**, which infers the cell morphological landscape tends to be more unstable at the

high doses (3μM). The non-monotonic trend of the characteristics such as the average cell length and the overlap rate infers that the "psychological activity" of the yeast is awakened gradually at the high doses, which is quantitatively confirmed by this net flux study. Considering that the higher the dose, the longer the "calming time", it seems that even if the polar growth was purposely reduced, the yeast still did not give up waiting for mating.

Finally, in order to prove the rationality of Fus3p's fluorescence double states, we developed a simplified signal transduction gene regulatory network model. The distributions in the two simulations, fluorescence intensity and cell morphology, were consistent with the experimental results and supported our proposed mechanisms. Thus far, we've quantified the global fate decisions made by yeast cells in response to sexual deception, and we've established the logical links between the functions of regulated proteins on the pheromone pathway for mating through the underlying signal transduction process.

Materials and Methods

Yeast strains and Growth media

The yeast strain used in this experiment is Saccharomyces cerevisiae S288C (ATCC 201388: *MAT*a *his*3Δ1 *leu*2Δ0 *met*15Δ0 *ura*3Δ0) **(Ghaemmaghami et al., 2003)**. In the yeast fluorescence library, we choose a special yeast as the research object, whose c-terminal of Fus3 is fused with GFP as the reporter protein. The yeasts are cultured by inoculating 5ml of YNB [Yeast Nitrogen Base Without Amino Acids

706 (6.8 g/L), Dextrose (5 g/L), Uracil (76mg/L), 50×MEM Amino Acids (20ml/L)]
707 medium with a colony from a YPD agar plate [Yeast extract (10 g/L), Peptone (20
708 g/L), Dextrose (20 g/L), Agar (10 g/L)]. Cells are grown overnight at 30℃ shaking at
709 250 rpm (about 14h). Before starting the experiment, we take out 20ul of overnight
710 cultures and dilute 100-fold in 2ml YNB medium to obtain an optical density of 0.1 at
711 600 nm (OD600nm).

712 **Pheromone environment**

713 The stimulus source we chose is pheromone, an alpha factor peptide hormone,
714 whose molecular weight is 1683.98 (GenScript). We weigh a certain amount of
715 powdered pheromone and dissolve them in YPD and YNB liquid medium
716 respectively to prepare 1000μM pheromone medium, and then gradually dilute it to
717 the ideal concentration medium for microscopy experiments and other experiments.

718 At the beginning, in order to adapt to the microfluidic environment, the yeast
719 cells are cultured in the YNB conventional medium for 60 minutes, and then are
720 switched to the medium supplemented with pheromone for culture.

721 **Flow cytometry**

722 To determine the critical concentration of pheromone, we chose a flow cytometer
723 for preliminary screening. We set 8 different concentrations (0.01μM, 0.05μM,
724 0.1μM, 0.2μM, 0.4μM, 0.6μM, 1.0μM, 1.5μM) for the pheromone medium, and
725 culture the yeast cells in a shaker at 250 rpm and 30℃. In order to avoid
726 contamination of the yeast cells, we have set up 5 sets of parallel culture samples for
727 each concentration of the medium. After culturing on a shaker for specific times (3h,

728 6h, 9h, 12h and 24h), 105,000 cells are taken from each sample for analysis using the
729 flow cytometer.

730 **Microfluidic system platform**

731 We use the 4-chamber cell culture plate, CellASIC™ ONIX Y04C-02
732 Microfluidic Plate, for live cell culture at 30°C. The plate is designed for use with the
733 CellASIC™ ONIX Microfluidic System, which provides a controlled dynamical
734 microenvironment for cells. First, the yeast cells are cultured in a microfluidic plate
735 containing conventional YNB medium for 1 hour to adapt to the new environment,
736 and then switch to YNB medium supplemented with pheromone and culture at a flow
737 rate of 1 psi for 30 hours.

738 **Microscopy Measurements**

739 The fluorescence values of the single cells were measured using an inverted
740 fluorescence microscopy (Ti-E, Nikon) with automated stage and focus, equipped
741 with a high NA oil-immersion objective (1.45NA, 100×). We applied 488nm laser
742 and set the output power at 30mW (only 10% of the laser beam into the microscope
743 objective), the fluorescence signals were collected by a cooled EM-CCD camera
744 (897U, Andor). All images were acquired using both bright field imaging and
745 fluorescent field imaging. These images were acquired by Nikon software. Data
746 analysis were accomplished through a combination of manual and automated analysis
747 using custom Matlab code. Many trajectories were taken from a time-lapse
748 microscopy. The fluorescent images were periodically captured and recorded every 10

749 minutes. The fluorescent data of each cell at each time point were collected for the
750 following discussion.

751 **Real time image analysis**

752 Bright-field images obtained by the total internal reflection microscope were
753 segmented, aligned, and labeled using a custom Matlab routine. We segmented the
754 cells according to bright field images to obtain the outlines of the individual cells, and
755 assigned each cell accordingly. Then we can collect the trajectories of the generations
756 by the assigned id when the cells grow and divide, and obtain cell lineages. All the
757 cell boundaries of yeast were manually corrected. The cell nuclei were distinguished
758 by contouring the fluorescence images. Fluorescence intensity is the average of all
759 fluorescence intensity within the cell boundary.

760 The real-time trajectories were obtained by automatic tracking, based on the cell
761 overlaps between the adjacent frames. All trajectories require manual correction.

762 **Steady-state image analysis**

763 In order to explore the underlying mechanism of the bimodality, we collected the
764 real time fluorescence intensity trajectories **(Figure 3–figure supplement 1, 2)**,
765 which show that the yeast response is in a steady state after about 600min. This state
766 means that the fluorescence intensity of the yeast inside and outside the nucleus does
767 not increase or decrease significantly. The histograms of inner and outer fluorescence
768 intensity were obtained by the steady-state fluorescence trajectories **(Figure 3–figure**
769 **supplement 3-5)**.

The shape characteristics of the yeast are described by the H_n in the yeast. The growth rate of the yeast is the numerical differentiation of the H_n. All the trajectories can be used to provide the quantitative analysis through Hidden Markov Chain Model (HMM). During the HMM fitting, the parameters of the fluorescence state were fixed. The distribution of high fluorescence state and low fluorescence state in two growth rates can be obtained by counting the state points on the trajectories.

Data Analysis of the Time-Lapse Experiments

The cell state can be distinguished from the trajectories using hidden Markov model (HMM). A maximum likelihood estimate of HMM parameters was performed globally on all the time traces separately. Multiple random initial parameters were used to start the iterative HMM analysis and ensure convergence to the global minimum. The Baum-Welch algorithm was used to re-estimate the parameters at the end of each iteration. Steady-state condition was enforced on the re-estimated parameters in each iteration. HMM can be directly applied to two-dimensional and high-dimensional data. Therefore, the inner and outer fluorescence data can be trained by the HMM, the results showed that the yeast fluorescence has bimodal distribution. The detailed results are shown in **Figure 4—source data 2 and Appendix 1—table 3, 4**. The overlap ratio between the two states is obtained by integrating the overlapping part of the peak of the two states, which needs the results fitted by HMM. For each trajectory, the state can be determined by the HMM, and the state sequence is shown in **Figure 3E**. The total residence time and the number of state changes can be obtained by counting the state points on the trajectories, and the average residence

792 time is the quotient of the total residence time and the number of state changes.

793

794 # Appendix 1

795 **The distinction between nucleus and cytoplasm**

796 To verify this dynamical understanding at the different pheromone doses, we had
797 to distinguish the nucleus in the cell. The fluorescence intensities of all pixels in the
798 single cells taken in each frame were plotted as a probability distribution over time
799 **(Figure 3–figure supplement 6)**. It can be seen from the figure that there are two
800 fluorescence intensity peaks in each cell at different time points. After adding the
801 pheromone, both peaks move to the right and the peak spacing is widened, indicating
802 that the increased expression of Fus3p tends to accumulate in the nucleus. Therefore,
803 we divided the two types of Fus3p fluorescence intensity in the cell by calculating the
804 contour of the fluorescent image. The contour images were calculated by four levels,
805 and the maximum level is the boundary of the nucleus and the cytoplasm. The
806 fluorescence greater than the threshold value was located inside the nucleus, and the
807 fluorescence smaller than the threshold value was located outside the nucleus.

808 **Filled circle model in cell shape**

809 After identifying the boundary of the cell shape with "Matlab", we filled it in
810 with circles along the cell's long axis in turns, with the area of the circle filled in each
811 time being guaranteed to be the largest area of the remaining unfilled part. To ensure
812 the accuracy of the average value of the harmony at various stages, we set a minimum
813 circle diameter (5 pixels) to avoid significantly increasing the shape's internal gap.

814 **Screening out the appropriate pheromone concentration**

815 By observing the yeast cells using a flow cytometer, the fluorescence intensity of
816 the Fus3-GFP was collected for statistical analysis. The emergence of the bimodal
817 states in the distribution of the fluorescence intensity of Fus3-GFP indicates that there

818 are two types of cells. One is the original undeformed cells (the initial mother cells at
819 the stage of "0-a" & the new daughter cells at the stage of "b-c" in the **Figure 2B**).
820 The other is the deformed cells (the deformed mother cells at the stage of "a-c" in the
821 **Figure 2B**).

822 Through the statistics of the data stimulated by different pheromone
823 concentrations, it is found that when the pheromone concentration is near 0.6μM, the
824 expressions of Fus3p begin to gradually show the emergence of bimodal states
825 **(Figure 2C)**. When the concentration is greater than 0.6μM (0.6-1.5μM), as the dose
826 increases, the number of the cells whose cell cycle is arrested by the pheromone that
827 resumes budding decrease accordingly. This leads to the gradual increase in the ratio
828 of the right peak representing the number of the deformed cells. It indicates that after
829 reaching the "adaptation steady state", the 0.6μM pheromone is the closest minimum
830 threshold to make the cells resume budding reproduction in the shortest time. In other
831 words, the fluorescence intensity of Fus3p in the yeast cells can reach the "adaptation
832 steady state" only if the concentration is greater than this concentration, so we choose
833 0.6μM as the critical pheromone concentration.

834 **Reasonable molecular mechanism of fluorescence double state**

835 Considering the molecular mechanism of Fus3p's expression, we believe that the
836 feedback regulation is the reason for the emergence of the $(L_1,\ L_2)$ & $(H_1,\ H_2)$ states.
837 For example, the mode of "A → Fus3p ┤A" mainly refers to the feedback adjustment
838 of Fus3p to itself through Sst2p, and the mode of "Fus3p → B ┤Fus3p" mainly refers
839 to the feedback adjustment of Fus3p to itself through Msg5p/Bni1p **(Figure 3D)**.
840 However, one may wonder why the states $(L_1,\ H_2)$ and $(H_1,\ L_2)$ do not appear in this
841 scheme. By calculating the "Pearson correlation coefficient" between the intranuclear
842 and extranuclear fluorescence intensity, the results show that the correlation is about
843 0.8 at different concentrations of pheromone **(Appendix 1—table 1)**. This confirms
844 that the fluorescence intensity of these two positions has a strong linear correlation. If
845 these two sets of data points are clustered into four states, the "Pearson correlation

coefficient" of the intranuclear and extranuclear fluorescence intensity will be 0 (Lee Rodgers and Nicewander, 1988), which provides the experimental evidence that the $(L_1,\ H_2)$ and $(H_1,\ L_2)$ states do not appear.

Derivation of the transition rates

The master equation can be written as

$$\frac{d}{dt}\begin{pmatrix}P_1\\P_2\end{pmatrix}=\begin{pmatrix}k_{11} & k_{12}\\k_{21} & k_{22}\end{pmatrix}\begin{pmatrix}P_1\\P_2\end{pmatrix}=\begin{pmatrix}-a & b\\a & -b\end{pmatrix}\begin{pmatrix}P_1\\P_2\end{pmatrix}.$$

Here P_1 and P_2 are the probabilities of the low expression state and high expression state, respectively, while k_{ij} (i, j=1, 2) is the transition rate from P_i to P_j. We can write down the solution as follows with the initial conditions $P_1(0)=1$, $P_2(0)=0$,

$$P_1(\mathrm{t})=\frac{b+a\,e^{-(a+b)t}}{a+b}$$

$$P_2(\mathrm{t})=-\frac{a(-1+e^{-(a+b)t})}{a+b}.$$

Then the transition probability between the low expression state and the low expression state is

$$P_{11}=P_1(\delta t)=\frac{b+a\,e^{-(a+b)\delta t}}{a+b},$$

where δt is the observational time window for each time, here $\delta t=10\ min$.

With the initial conditions $P_1(0)=0$, $P_2(0)=1$,

$$P_1(\mathrm{t})=-\frac{\mathrm{b}(-1+\ e^{-(a+b)t})}{a+b}$$

$$P_2(\mathrm{t})=\frac{a+b\,e^{-(a+b)t}}{a+b}.$$

Then the transition probability between the high expression state and the high expression state is

$$P_{22}=P_2(\delta t)=\frac{a+b\,e^{-(a+b)\delta t}}{a+b},$$

where δt is the observation time window for each time, here $\delta t=10\ min$.

According to the HMM analysis, when the pheromone dose is 0.7μM, the transition matrix is

$$\mathrm{P}=\begin{pmatrix}P_{11} & P_{12}\\P_{21} & P_{22}\end{pmatrix}=\begin{pmatrix}0.6900 & 0.3100\\0.3711 & 0.6289\end{pmatrix}.$$

So we can get the transition rate as:

870 a= 0.052017 (1/min)

871 b= 0.062270 (1/min)

872 **Justification for cellular morphological characterization**

873 Rather than using the cell's area, the total length, or the arithmetic mean of the
874 length, we chose to describe the cell's morphology using the reciprocal of the radius
875 in the cell-filled circle multiplied by the number of filled circles, i.e. $H_n = nR_{ij} =$
876 $n\left(\frac{1}{R_1} + \frac{1}{R_2} + \cdots + \frac{1}{R_n}\right)$. This is because H_n bears a resemblance to the harmonic mean.
877 It is capable of not only displaying changes in various positions more
878 comprehensively, but also distinguishing between longitudinal or lateral growth
879 processes. For example, we set the radius of the filled circle in the cell as R_1, R_2 and
880 R_3 in advance. If the cell grows longitudinally (length), a new radius R_4 is added to
881 the cell, the R_{ij} value increases, and the H_n value increases as well. By contrast, when
882 the cell grows laterally (width), the values of R_{ij} and H_n decrease regardless of the
883 radius that grows.

884 **Detailed description of the four molecular mechanisms of the growth rates**

885 As we know from its internal activities, there are two pathways that can lead to
886 the polar growth of the cells. The path1 ("P_1") is "Fus3p → Far1p/Cdc24p → Cdc42p
887 → Bni1p" **(Butty *et al.*, 1998; Nern and Arkowitz, 1999; 2000b; Shimada *et al.*,**
888 **2000)**. It is realized by entering nucleus through Fus3p to activate Far1, which can
889 escape from the nucleus to activate Bni1p indirectly. The path2 ("P_2") is for Fus3p to
890 directly activate Bni1p in the cytoplasm, namely "Fus3p → Bni1p" **(Matheos *et al.*,**
891 **2004)**. Many studies have shown that Fus3p and Far1p were both important genes for
892 the formation of the cell growth axis determined by the bud site and the mutants.
893 Lacking of Far1p or Fus3p would cause the mis-localization of the shmoo projections
894 **(Butty *et al.*, 1998; Nern and Arkowitz, 1999; 2000a)**. Therefore, we suggest that
895 the "P_1" is more directional than the "P_2" (longitudinal growth) **(Figure 3C)**.

When the fluorescence intensity is in the "high state", the Fus3p can indirectly ("P_1") or directly ("P_2") stimulate growth. However, the response speed of the two pathways to the polar growth process is not the same. In the cell's indirect growth pathway ("P_1"), Far1p can transfer from the nucleus to the vicinity of the cell membrane and gives the cell more polar direction for growth together with Fus3p. When the Fus3p activates the Far1p in the nucleus, the process by which the Far1p transmits the signal to the cytoplasm and indirectly leads to the polar growth of the cells ("P_1") is naturally slower than the polar growth directly stimulated by Fus3p ("P_2"). Therefore, before all the indirect pathway signals transmitted by Far1p arrive, it is mainly the extranuclear Fus3p that activates the cell's polar growth gene Bni1p ("P_1"), which will lead to the non-directional cell growth temporarily.

If all the signals of the indirect pathway arrive, the two growth pathways will co-stimulate the polar growth of the cell ("$P_1 + P_2$"). In other words, the participation of the indirect pathway "P_1", that is ("$P_1 + P_2$"), greatly increases the probability of the cell polar growth. Therefore, we believe that the lateral growth of the cell is mainly caused by the direct pathway ("P_2"), while the longitudinal growth of the cells is caused by the combined action of these two pathways ("$P_1 + P_2$"). In addition, with the consumption of polarity growth and the adjustment of negative feedback, the fluorescence intensity of Fus3p will enter the "low state" waiting for mating. Correspondingly, only a relatively small amount of Fus3p is used for polar growth of the cells at this stage. In this case, the signal transmission of the indirect path ("P_0" and "P_1") with the insignificant growth rates also has a certain time delay.

Relationship between the growth rate and the bistable gene expressions

The "High & Low" fluorescence states exist in both two growth rates. One of the reasons for this is that the growth rate is a characteristic of the cell behavior indirectly caused by Fus3p, the amount of Fus3p used for growth is not consistent with the total fluorescence intensity observed. Therefore, the expression of Fus3p is related to cell growth rate to a certain extent, but not necessarily in a completely linear manner,

which explains why the two are neither independent nor exactly correlated. The other most important reason for above is the overlapping effect of the dual fluorescence states. From the fitting process of the fluorescence two-state, we know that there is certain amount of mixed data in the main part of the "two hills" **(Figure 3B)**. In the overlapping area of the "two hills", the fluorescence intensity of the "High-state" is not necessarily higher than that of the "Low-state", for example, the fluorescence intensity of the "b-point" in the "Low-state" is greater than the "a-point" in the "High-state" (**Figure 6C).**

In order to better describe the overlapping effect of the fluorescence data, we draw a schematic diagram to explain the mixed area of the fluorescence intensity **(Figure 6–figure supplement 4).** Meanwhile, if we want to distinguish the state of the fluorescence intensity in the overlapping area (such as the "a" intensity in the **Figure 6C**), we need to compare the probability that the intensity belongs to the high state or the low state, that is, f_0 or f_1 multiplied by their respective transition probabilities. As a result, the large fluorescence intensity has certain probability of belonging to the "Low-state", on the contrary, the small fluorescence intensity also has certain probability of belonging to the "High-state". Therefore, the "*FL*" represents the state of "Fast" growth rate and "Large-intensity" in the "Low-state" fluorescence; the "*SH*" represents the state of "Slow" growth rate and "Small-intensity" in the "High-state" fluorescence.

Decomposing of the flux in the cell morphology

The kinetics of the cell morphological can be modeled by a four-state Markov process. The transition probability (M_{ij}) can be calculated by counting the number of transitions in the state trajectories. Therefore, the master equation can be shown as follows:

$$\frac{dP_i}{dt} = \sum_j M_{ij} P_i \qquad \textbf{(Equation 1)}$$

Where P_i represents the probability of state i, and the transition probability M_{ij} represents the transition probability from state i to state j. For steady state, we set the

left term of the master equation (1) to zero, then we obtain the steady state solution P_i^S, which is the long time limit. The steady state flux between state i and j can be defined as: $F_{ij} = -M_{ij}P_i^S + M_{ji}P_j^S$. If the steady state of the system is in equilibrium state, the flux between any two nodes in the system is zero, that is the detailed balance condition. For the general biological system, it does not necessarily satisfy the detailed balance condition ($F_{ij} \neq 0$), the system is in non-equilibrium steady state, there will be at least one net flux among states.

In order to study the non-equilibrium steady states, we can separate the dynamical process into two parts, one is the detailed balance part and the other is the detailed balance-breaking kinetic process. To describe the detailed balance breaking, we decompose the probability matrix. The component of the rate matrix MP can be decomposed into two parts, one being the symmetric matrix and the other cycle matrix, that is

$$MP = C + D \qquad \textbf{(Equation 2)}$$

Where D is the symmetric matrix $D_{ij} = \left(M_{ij}P_i^S + M_{ji}P_j^S\right)/2$, C is the asymmetric matrix $C_{ij} = \left(M_{ij}P_i^S - M_{ji}P_j^S\right)/2$. Since the system contains four states, the asymmetric flux is not unique and contains three net cycle fluxes. Meanwhile, in order to ensure the consistency of decomposition for various pheromone concentration systems, the given base sets of flux decomposition were selected. Here, the base sets we selected are {state1, state2, state3, state1}, {state1, state4, state3, state1} and {state2, state4, state3, state2}, and the corresponding net fluxes are J_1, J_2 and J_3. The asymmetric matrix C can be rewritten as follows:

$$C = \begin{pmatrix} 0 & \frac{J_1}{2} & -\frac{J_2}{2} - \frac{J_1}{2} & \frac{J_2}{2} \\ -\frac{J_1}{2} & 0 & \frac{J_1}{2} - \frac{J_3}{2} & \frac{J_3}{2} \\ \frac{J_1}{2} + \frac{J_2}{2} & -\frac{J_1}{2} + \frac{J_3}{2} & 0 & -\frac{J_2}{2} - \frac{J_3}{2} \\ -\frac{J_2}{2} & -\frac{J_3}{2} & \frac{J_2}{2} + \frac{J_3}{2} & 0 \end{pmatrix}$$

The linear equations can be obtained by corresponding the numerical results of the above matrix C and the experimental statistics **(Figure 7—source data 3-7)**. For example, three linearly independent parameters of $C_{1,4}, C_{1,3}, C_{2,3}$ are selected for the linear equations originated from the underlying master equations.

The linear equations(0.7μM) are $\begin{pmatrix} C_{1,4} = \frac{J_2}{2} = 0.0036 \\ C_{1,3} = -\frac{J_2}{2} - \frac{J_1}{2} = -0.0067 \\ C_{2,3} = \frac{J_1}{2} - \frac{J_3}{2} = 0 \end{pmatrix}$

Then, solving these linear equations one can get the net flux values of the non-equilibrium system.

983 **Appendix 1—table 1**

984 The "Pearson Correlation Coefficient" between the intranuclear and extranuclear

985 fluorescence intensity traces under the different pheromone doses.

Pheromone doses (μM)	**0.7**	**0.8**	**1.0**	**2.0**	**3.0**
Correlation (inside & outside)	0.8321	0.8647	0.8446	0.7752	0.8879

986

987 **Appendix 1—table 2**

988 The correlation between cell growth rate and dual state of fluorescence data under the

989 different pheromone doses.

Pheromone doses (μM)	**0.7**	**0.8**	**1.0**	**2.0**	**3.0**
Correlation (Growth rate & Fluorescence)	0.0298	-0.0069	0.011	0.023	0.0059

990

991 **Appendix 1—table 3**

992 Proportional distribution of high fluorescence state and low fluorescence state in two

993 growth rates.

Pheromone doses (μM)	**FH%**	**FL%**	**Number (FH+FL)**	**SH%**	**SL%**	**Number (SH+SL)**
0.7	0.9101	0.0899	11816	0.5752	0.4248	9519
0.8	0.9651	0.0349	7367	0.6278	0.3722	11041
1.0	0.9994	0.0006	9463	0.7302	0.2698	13578
2.0	0.6228	0.3772	6095	0.4749	0.5251	30791
3.0	0.2189	0.7811	1110	0.2215	0.7785	17166

994

995

996

997

998 **Appendix 1—table 4**

999 The weight distribution of the four combination states and the overlap ratio of

1000 Fluorescence intensity under the different pheromone doses.

Pheromone doses (μM)	**Overlap ratio (w)**	**$(\gamma_{FL}+\gamma_{SH})\%$ (w')**	γ_{FL}	γ_{FH}	γ_{SL}	γ_{SH}
0.7	0.3317	0.3064	0.0498	0.5041	0.1895	0.2566
0.8	0.3712	0.3905	0.0140	0.3862	0.2233	0.3765
1.0	0.4659	0.4305	0.0003	0.4104	0.1590	0.4303
2.0	0.4348	0.4588	0.0623	0.1029	0.4383	0.3964
3.0	0.2400	0.2555	0.0474	0.0133	0.7312	0.2080

1001

1002 **Appendix 1—table 5**

1003 The description of the components in the biochemical reactions.

Name	**Description**
$G*$	The gene of the $*$
$P*$	The protein of the $*$
$P*_p$	Phosphorylated protein of the $*$
$(P*_p)'$	The $P*_p$ remaining after the chemical reaction
$P*_p$ _inner	The $P*_p$ in the nucleus
$P*_p$ _outer	The $P*_p$ outside the nucleus
$P*_p$ _in	The $P*_p$ produced by the "P_1" pathway in the nucleus
$P*_p$ _out	The $P*_p$ produced by the "P_2" pathway outside the nucleus
$P*$ -B	This indicates the $P*_p$ produced by the action of the B
$G*$ -self	The $G*$ produced by its self-activation
Φ	Protein degradation

1004

1005

1006 **Appendix 1—table 6**

1007 The list of the components in the biochemical reactions.

1	*G*Fus3	**21**	*G*Fus3-*P*Msg5p
2	(*G*Fus3)'	**22**	(*G*Fus3-*P*Msg5p)'
3	*P*Fus3p_outer	**23**	*G*Far1
4	*pheromone*	**24**	(*G*Far1)'
5	*G*Fus3-pheromone	**25**	*P*Far1p
6	(*G*Fus3-pheromone)'	**26**	*G*Far1p-*P*Fus3p_inner
7	*G*Fus3-self	**27**	(*G*Far1-*P*Fus3p_inner)'
8	(*G*Fus3-self)'	**28**	*G*Bni1
9	*P*Fus3p_inner	**29**	(*G*Bni1)'
10	∅	**30**	*P*Bni1p
11	*G*Ste12	**31**	*G*Fus3_outer-*P*Bni1p
12	(*G*Ste12)'	**32**	(*G*Fus3_outer-*P*Bni1p)'
13	*P*Ste12p	**33**	*G*Bni1_in
14	*G*Ste12-*P*Fus3p_inner	**34**	*G*Bni1_in-*P*Far1p
15	(*G*Ste12-*P*Fus3p_inner)'	**35**	(*G*Bni1_in-*P*Far1p)'
16	*G*Msg5	**36**	*P*Bni1p_in
17	(*G*Msg5)'	**37**	*G*Bni1_out
18	*P*Msg5p	**38**	*G*Bni1_out-*P*Fus3p_outer
19	*G*Msg5-*P*Ste12p	**39**	(*G*Bni1_out-*P*Fus3p_outer)'
20	(*G*Msg5-*P*Ste12p)'	**40**	*P*Bni1p_out

1008

1009

Appendix 1—table 7

The list of the biochemical reactions.

1	$GFus3 \xrightarrow{k_1=1} (GFus3)' + (PFus3p\_outer)$
2	$GFus3 + pheromone \xrightarrow{k_2=0.7} (GFus3\text{-}pheromone)$
3	$(GFus3\text{-}pheromone) \xrightarrow{k_3=0.001} GFus3 + pheromone$
4	$(GFus3\text{-}pheromone) \xrightarrow{k_4=1.5} (GFus3\text{-}pheromone)' + (PFus3p\_outer)$
5	$GFus3 + (PFus3p\_outer) \xrightarrow{k_5=0.7} (GFus3\text{-}self)$
6	$(GFus3\text{-}self) \xrightarrow{k_6=0.001} GFus3 + (PFus3p\_outer)$
7	$(GFus3\text{-}self) \xrightarrow{k_7=1.5} (GFus3\text{-}self)' + (PFus3p\_outer)$
8	$(PFus3p\_outer) \xrightarrow{k_8=3.7} (PFus3p\_inner)$
9	$(PFus3p\_inner) \xrightarrow{k_9=3.7} (PFus3p\_outer)$
10	$(PFus3p\_outer) \xrightarrow{k_{10}=0.01} \varnothing$
11	$(PFus3p\_inner) \xrightarrow{k_{11}=0.01} \varnothing$
12	$GSte12 \xrightarrow{k_{12}=1} (GSte12)' + PSte12p$
13	$GSte12 + (PFus3p\_inner) \xrightarrow{k_{13}=0.7} (GSte12\text{-}PFus3p\_inner)$
14	$(GSte12\text{-}PFus3p\_inner) \xrightarrow{k_{14}=0.001} GSte12 + (PFus3p\_inner)$
15	$(GSte12\text{-}PFus3p\_inner) \xrightarrow{k_{15}=1.5} (GSte12\text{-}PFus3p\_inner)' + PSte12p$
16	$GMsg5 \xrightarrow{k_{16}=1} (GMsg5)' + PMsg5p$
17	$GMsg5 + PSte12p \xrightarrow{k_{17}=0.7} (GMsg5\text{-}PSte12p)$
18	$(GMsg5\text{-}PSte12p) \xrightarrow{k_{18}=0.001} GMsg5 + PSte12p$
19	$(GMsg5\text{-}PSte12p) \xrightarrow{k_{19}=1.2} (GMsg5\text{-}PSte12p)' + PMsg5p$
20	$GFus3 + PMsg5p \xrightarrow{k_{20}=0.7} (GFus3\text{-}PMsg5p)$
21	$(GFus3\text{-}PMsg5p) \xrightarrow{k_{21}=0.001} GFus3 + PMsg5p$
22	$(GFus3\text{-}PMsg5p) \xrightarrow{k_{22}=0.5} (GFus3\text{-}PMsg5p)' + (PFus3p\_outer)$
23	$(PSte12p) \xrightarrow{k_{23}=0.01} \varnothing$
24	$(PMsg5p) \xrightarrow{k_{24}=0.01} \varnothing$
25	$GFar1 \xrightarrow{k_{25}=1} (GFar1)' + PFar1p$
26	$GFar1 + (PFus3p\_inner) \xrightarrow{k_{26}=0.7} (GFar1p\text{-}PFus3p\_inner)$
27	$(GFar1p\text{-}PFus3p\_inner) \xrightarrow{k_{27}=0.001} GFar1 + (PFus3p\_inner)$
28	$(GFar1\text{-}PFus3p\_inner) \xrightarrow{k_{28}=1.5} (GFar1\text{-}PFus3p\_inner)' + (PFar1p)$
29	$(PFar1p) \xrightarrow{k_{29}=0.01} \varnothing$
30	$GBni1 \xrightarrow{k_{30}=0.1} (GBni1)' + PBni1p$

31	$G\text{Fus3\_outer} + P\text{Bni1p} \xrightarrow{k_{31}=0.7} (G\text{Fus3\_outer-}P\text{Bni1p})$
32	$(G\text{Fus3\_outer-}P\text{Bni1p}) \xrightarrow{k_{32}=0.001} G\text{Fus3\_outer} + P\text{Bni1p}$
33	$(G\text{Fus3\_outer-}P\text{Bni1p}) \xrightarrow{k_{33}=0.5} (G\text{Fus3\_outer-}P\text{Bni1p})' + (P\text{Fus3p\_outer})$
34	$(G\text{Bni1\_in}) + P\text{Far1p} \xrightarrow{k_{34}=0.7} (G\text{Bni1\_in-}P\text{Far1p})$
35	$(G\text{Bni1\_in-}P\text{Far1p}) \xrightarrow{k_{35}=0.7} (G\text{Bni1\_in}) + P\text{Far1p}$
36	$(G\text{Bni1\_in-}P\text{Far1p}) \xrightarrow{k_{36}=1.5} (G\text{Bni1\_in-}P\text{Far1p})' + (P\text{Bni1p\_in})$
37	$(G\text{Bni1\_out}) + (P\text{Fus3p\_outer}) \xrightarrow{k_{37}=0.7} (G\text{Bni1\_out-}P\text{Fus3p\_outer})$
38	$(G\text{Bni1\_out-}P\text{Fus3p\_outer}) \xrightarrow{k_{38}=0.7} (G\text{Bni1\_out}) + (P\text{Fus3p\_outer})$
39	$(G\text{Bni1\_out-}P\text{Fus3p\_outer}) \xrightarrow{k_{39}=1.5} (G\text{Bni1\_out-}P\text{Fus3p\_outer})' + (P\text{Bni1p\_out})$
40	$(P\text{Bni1p\_out}) \xrightarrow{k_{40}=0.01} \varnothing$
41	$(P\text{Bni1p\_in}) \xrightarrow{k_{41}=0.01} \varnothing$

Appendix 2

Figure 2–videos 1-6 legends: Total internal reflection microscopy images of yeast cell morphology in response to 0.6μM, 0.7μM, 0.8μM, 1.0μM, 2.0μM, and 3.0μM pheromones over time. The shooting interval of the photos was 10 minutes/frame. Yeast cells were cultured in a microfluidic device containing the normal YNB medium for 60 minutes, and then switched to the medium containing a specific concentration of pheromone for cultivation. The green fluorescence in the cell is the gene expression level of Fus3p.

Acknowledgements

This work was supported by the National Natural Science Foundation of China with Grant No.21721003.

References

Anders, A., Ghosh, B., Glatter, T., and Sourjik, V. (2020). Design of a MAPK signalling cascade balances energetic cost versus accuracy of information transmission. Nature communications *11*, 1-10.

Anne-Christine Butty, P.M.P., Linda S. Huang, Ira Herskowitz, Matthias Peter* (1998). The Role of Far1p in Linking the Heterotrimeric G Protein to Polarity Establishment Proteins During Yeast Mating. SCIENCE.

Balázsi, G., van Oudenaarden, A., and Collins, J.J. (2011). Cellular decision making and biological noise: from microbes to mammals. Cell *144*, 910-925.

Bao, M.Z., Schwartz, M.A., Cantin, G.T., Yates III, J.R., and Madhani, H.D. (2004). Pheromone-dependent destruction of the Tec1 transcription factor is required for MAP kinase signaling specificity in yeast. Cell *119*, 991-1000.

Bar-Joseph, Z., Gitter, A., and Simon, I. (2012). Studying and modelling dynamic biological processes using time-series gene expression data. Nature Reviews Genetics *13*, 552-564.

Bardwell, L. (2004). A walk-through of the yeast mating pheromone response pathway. Peptides *25*, 1465-1476. 10.1016/j.peptides.2003.10.022.

Bardwell, L. (2005). A walk-through of the yeast mating pheromone response pathway (vol 25, pg 1465, 2004). Peptides *26*, 337-+. 10.1016/j.peptides.2004.10.001.

Barkai, N., Rose, M.D., and Wingreen, N.S. (1998). Protease helps yeast find mating partners. Nature *396*, 422-423.

Behar, M., Hao, N., Dohlman, H.G., and Elston, T.C. (2008). Dose-to-Duration Encoding and Signaling beyond Saturation in Intracellular Signaling Networks. Plos Computational Biology *4*. ARTN e1000197
10.1371/journal.pcbi.1000197.

Berg, H.C., and Brown, D.A. (1972). Chemotaxis in Escherichia coli analysed by three-dimensional tracking. Nature *239*, 500-504.

Bhattacharyya, R.P., Reményi, A., Good, M.C., Bashor, C.J., Falick, A.M., and Lim, W.A. (2006). The Ste5 scaffold allosterically modulates signaling output of the yeast mating pathway. Science *311*, 822-826.

Blackwell, E., Halatek, I.M., Kim, H.-J.N., Ellicott, A.T., Obukhov, A.A., and Stone, D.E. (2003). Effect of the pheromone-responsive Gα and phosphatase proteins of Saccharomyces cerevisiae on the subcellular localization of the Fus3 mitogen-activated protein kinase. Molecular and cellular biology *23*, 1135-1150.

Butty, A.-C., Pryciak, P.M., Huang, L.S., Herskowitz, I., and Peter, M. (1998). The role of Far1p in linking the heterotrimeric G protein to polarity establishment proteins during yeast mating. Science *282*, 1511-1516.

Chang, F., and Herskowitz, I. (1990). Identification of a gene necessary for cell cycle arrest by a negative growth factor of yeast: FAR1 is an inhibitor of a G1 cyclin, CLN2. Cell *63*, 999-1011.

Chen, R.E., and Thorner, J. (2007). Function and regulation in MAPK signaling pathways: Lessons learned from the yeast Saccharomyces cerevisiae. Bba-Mol Cell Res *1773*, 1311-1340. 10.1016/j.bbamcr.2007.05.003.

Chen, T., and Kurjan, J. (1997). Saccharomyces cerevisiae Mpt5p interacts with Sst2p and plays roles in pheromone sensitivity and recovery from pheromone arrest. Molecular and Cellular Biology *17*, 3429-3439.

Colman-Lerner, A., Gordon, A., Serra, E., Chin, T., Resnekov, O., Endy, D., Gustavo Pesce, C., and Brent, R. (2005a). Regulated cell-to-cell variation in a cell-fate decision system. Nature *437*, 699-706.

Colman-Lerner, A., Gordon, A., Serra, E., Chin, T., Resnekov, O., Endy, D., Pesce, C.G., and Brent, R. (2005b). Regulated cell-to-cell variation in a cell-fate decision system. Nature *437*, 699-706.

Davidson, E.H., and Erwin, D.H. (2006). Gene regulatory networks and the evolution of animal body plans. Science *311*, 796-800.

De Jong, H. (2002). Modeling and simulation of genetic regulatory systems: a literature review. Journal of computational biology *9*, 67-103.

De Oliveira, S., Rosowski, E.E., and Huttenlocher, A. (2016). Neutrophil migration in infection and wound repair: going forward in reverse. Nature Reviews Immunology *16*, 378.

Dohlman, H.G., Song, J., Ma, D., Courchesne, W.E., and Thorner, J. (1996). Sst2, a negative regulator of pheromone signaling in the yeast Saccharomyces cerevisiae: expression, localization, and genetic interaction and physical association with Gpa1 (the G-protein alpha subunit). Molecular and cellular biology *16*, 5194-5209.

Dohlman, H.G., and Thorner, J.W. (2001). Regulation of G protein-initiated signal transduction in yeast: Paradigms and principles. Annu Rev Biochem *70*, 703-754. DOI 10.1146/annurev.biochem.70.1.703.

Doncic, A., Atay, O., Valk, E., Grande, A., Bush, A., Vasen, G., Colman-Lerner, A., Loog, M., and Skotheim, J.M. (2015). Compartmentalization of a Bistable Switch Enables Memory to Cross a Feedback-Driven Transition. Cell *160*, 1182-1195. 10.1016/j.cell.2015.02.032.

Doncic, A., Falleur-Fettig, M., and Skotheim, J.M. (2011). Distinct interactions select and maintain a specific cell fate. Molecular cell *43*, 528-539.

Dworkin, J. (2009). Cellular Polarity in Prokaryotic Organisms. Csh Perspect Biol *1*. ARTN a003368
10.1101/cshperspect.a003368.

Elion, E., Satterberg, B., and Kranz, J. (1993). FUS3 phosphorylates multiple components of the mating signal transduction cascade: evidence for STE12 and FAR1. Molecular biology of the cell *4*, 495-510.

Elion, E.A., Brill, J.A., and Fink, G.R. (1991). FUS3 represses CLN1 and CLN2 and in concert with KSS1 promotes signal transduction. Proceedings of the National Academy of Sciences *88*, 9392-9396.

Elion, E.A., Qi, M., and Chen, W. (2005). Signaling specificity in yeast. Science *307*, 687-688.

Errede, B., Gartner, A., Zhou, Z., Nasmyth, K., and Ammerer, G. (1993). MAP kinase-related FUS3 from S. cerevisiae is activated by STE7 in vitro. Nature *362*, 261-264.

Fang, X., Kruse, K., Lu, T., and Wang, J. (2019). Nonequilibrium physics in biology.

Reviews of Modern Physics *91*, 045004.
Fang, X., Liu, Q., Bohrer, C., Hensel, Z., Han, W., Wang, J., and Xiao, J. (2018a). Cell fate potentials and switching kinetics uncovered in a classic bistable genetic switch. Nature communications *9*, 1-9.
Fang, X.N., Liu, Q., Bohrer, C., Hensel, Z., Han, W., Wang, J., and Xiao, J. (2018b). Cell fate potentials and switching kinetics uncovered in a classic bistable genetic switch. Nature Communications *9*. ARTN 2787
10.1038/s41467-018-05071-1.
Feng, H., and Wang, J. (2011). Potential and flux decomposition for dynamical systems and non-equilibrium thermodynamics: Curvature, gauge field, and generalized fluctuation-dissipation theorem. The Journal of chemical physics *135*, 234511.
Feng, H., Zhang, K., and Wang, J. (2014). Non-equilibrium transition state rate theory. Chemical Science *5*, 3761-3769.
Fiedler, D., Braberg, H., Mehta, M., Chechik, G., Cagney, G., Mukherjee, P., Silva, A.C., Shales, M., Collins, S.R., and van Wageningen, S. (2009). Functional organization of the S. cerevisiae phosphorylation network. Cell *136*, 952-963.
Garrison, T.R., Zhang, Y., Pausch, M., Apanovitch, D., Aebersold, R., and Dohlman, H.G. (1999). Feedback phosphorylation of an RGS protein by MAP kinase in yeast. Journal of Biological Chemistry *274*, 36387-36391.
Ghaemmaghami, S., Huh, W.-K., Bower, K., Howson, R.W., Belle, A., Dephoure, N., O'Shea, E.K., and Weissman, J.S. (2003). Global analysis of protein expression in yeast. Nature *425*, 737-741.
Gillespie, D.T. (2000). The chemical Langevin equation. The Journal of Chemical Physics *113*, 297-306.
Gillespie, D.T. (2001). Approximate accelerated stochastic simulation of chemically reacting systems. The Journal of chemical physics *115*, 1716-1733.
Gordley, R.M., Williams, R.E., Bashor, C.J., Toettcher, J.E., Yan, S., and Lim, W.A. (2016). Engineering dynamical control of cell fate switching using synthetic phospho-regulons. P Natl Acad Sci USA *113*, 13528-13533. 10.1073/pnas.1610973113.
Gustin, M.C., Albertyn, J., Alexander, M., and Davenport, K. (1998). MAP Kinase Pathways in the YeastSaccharomyces cerevisiae. Microbiology and Molecular biology reviews *62*, 1264-1300.
Haber, J.E. (2012). Mating-type genes and MAT switching in Saccharomyces cerevisiae. Genetics *191*, 33-64.
Hasty, J., McMillen, D., Isaacs, F., and Collins, J.J. (2001). Computational studies of gene regulatory networks: in numero molecular biology. Nature Reviews Genetics *2*, 268-279.
Herskowitz, I. (1988). Life cycle of the budding yeast Saccharomyces cerevisiae. Microbiological reviews *52*, 536.
Herskowitz, I. (1995). MAP kinase pathways in yeast: for mating and more. Cell *80*, 187-197.
Hull, C.M., Raisner, R.M., and Johnson, A.D. (2000). Evidence for mating of the" asexual" yeast Candida albicans in a mammalian host. Science *289*, 307-310.

Jenness, D.D., Burkholder, A.C., and Hartwell, L.H. (1983). Binding of α-factor pheromone to yeast a cells: chemical and genetic evidence for an α-factor receptor. Cell *35*, 521-529.

Jiang, Z., Tian, L., Fang, X., Zhang, K., Liu, Q., Dong, Q., Wang, E., and Wang, J. (2019a). The emergence of the two cell fates and their associated switching for a negative auto-regulating gene. BMC biology *17*, 1-14.

Jiang, Z.L., Tian, L., Fang, X.N., Zhang, K., Liu, Q., Dong, Q.Z., Wang, E.K., and Wang, J. (2019b). The emergence of the two cell fates and their associated switching for a negative auto-regulating gene. Bmc Biology *17*. ARTN 49 10.1186/s12915-019-0666-0.

Kedrin, D., van Rheenen, J., Hernandez, L., Condeelis, J., and Segall, J.E. (2007). Cell motility and cytoskeletal regulation in invasion and metastasis. Journal of mammary gland biology and neoplasia *12*, 143-152.

Kőhidai, L. (1999). Chemotaxis: the proper physiological response to evaluate phylogeny of signal molecules. Acta Biologica Hungarica *50*, 375-394.

Kranz, J.E., Satterberg, B., and Elion, E.A. (1994). The MAP kinase Fus3 associates with and phosphorylates the upstream signaling component Ste5. Genes & Development *8*, 313-327.

Laviña, W.A., Sugiyama, M., Kaneko, Y., and Harashima, S. (2010). Identification of protein kinase disruptions as suppressors of the calcium sensitivity of S. cerevisiae Δ ptp2 Δ msg5 protein phosphatase double disruptant. Archives of microbiology *192*, 157-165.

Laviña, W.A., Sugiyama, M., Kaneko, Y., and Harashima, S. (2013). Functionally redundant protein phosphatase genes PTP2 and MSG5 co-regulate the calcium signaling pathway in Saccharomyces cerevisiae upon exposure to high extracellular calcium concentration. Journal of bioscience and bioengineering *115*, 138-146.

Lee Rodgers, J., and Nicewander, W.A. (1988). Thirteen ways to look at the correlation coefficient. The American Statistician *42*, 59-66.

Levine, H., and Rappel, W.-J. (2013). The physics of eukaryotic chemotaxis. Physics today *66*.

Li, C., Wang, E., and Wang, J. (2011). Landscape, flux, correlation, resonance, coherence, stability, and key network wirings of stochastic circadian oscillation. Biophysical journal *101*, 1335-1344.

Li, C., and Wang, J. (2014). Landscape and flux reveal a new global view and physical quantification of mammalian cell cycle. Proceedings of the National Academy of Sciences *111*, 14130-14135. 10.1073/pnas.1408628111.

Macnab, R.M., and Koshland, D.E. (1972). The gradient-sensing mechanism in bacterial chemotaxis. Proceedings of the National Academy of Sciences *69*, 2509-2512.

Maeder, C.I., Hink, M.A., Kinkhabwala, A., Mayr, R., Bastiaens, P.I., and Knop, M. (2007). Spatial regulation of Fus3 MAP kinase activity through a reaction-diffusion mechanism in yeast pheromone signalling. Nature cell biology *9*, 1319-1326.

Malleshaiah, M.K., Shahrezaei, V., Swain, P.S., and Michnick, S.W. (2010). The scaffold protein Ste5 directly controls a switch-like mating decision in yeast. Nature

465, 101-105.
Marsh, L., and Rose, M. (1997). The pathway of cell and nuclear fusion during mating in S. cerevisiae. COLD SPRING HARBOR MONOGRAPH SERIES *21*, 827-888.
Matheos, D., Metodiev, M., Muller, E., Stone, D., and Rose, M.D. (2004). Pheromone-induced polarization is dependent on the Fus3p MAPK acting through the formin Bni1p. The Journal of cell biology *165*, 99-109.
Molk, J.N., and Bloom, K. (2006). Microtubule dynamics in the budding yeast mating pathway. Journal of cell science *119*, 3485-3490.
Neiman, A.M., and Herskowitz, I. (1994). Reconstitution of a Yeast Protein-Kinase Cascade in-Vitro - Activation of the Yeast Mek Homolog Ste7 by Ste11. P Natl Acad Sci USA *91*, 3398-3402. DOI 10.1073/pnas.91.8.3398.
Nern, A., and Arkowitz, R.A. (1999). A Cdc24p-Far1p-Gβγ protein complex required for yeast orientation during mating. The Journal of cell biology *144*, 1187-1202.
Nern, A., and Arkowitz, R.A. (2000a). G proteins mediate changes in cell shape by stabilizing the axis of polarity. Molecular cell *5*, 853-864.
Nern, A., and Arkowitz, R.A. (2000b). Nucleocytoplasmic shuttling of the Cdc42p exchange factor Cdc24p. The Journal of cell biology *148*, 1115-1122.
Norris, D., and Osley, M. (1987). The two gene pairs encoding H2A and H2B play different roles in the Saccharomyces cerevisiae life cycle. Molecular and Cellular Biology *7*, 3473-3481.
Parnell, S.C., Marotti, L.A., Kiang, L., Torres, M.P., Borchers, C.H., and Dohlman, H.G. (2005). Phosphorylation of the RGS protein Sst2 by the MAP kinase Fus3 and use of Sst2 as a model to analyze determinants of substrate sequence specificity. Biochemistry *44*, 8159-8166.
Peter, M., Gartner, A., Horecka, J., Ammerer, G., and Herskowitz, I. (1993). FAR1 links the signal transduction pathway to the cell cycle machinery in yeast. Cell *73*, 747-760.
Roberts, R.L., and Fink, G.R. (1994). Elements of a single MAP kinase cascade in Saccharomyces cerevisiae mediate two developmental programs in the same cell type: mating and invasive growth. Genes & development *8*, 2974-2985.
Rose, M.D. (1996). Nuclear fusion in the yeast Saccharomyces cerevisiae. Annu Rev Cell Dev Bi *12*, 663-695.
Segall, J.E. (1993). Polarization of yeast cells in spatial gradients of alpha mating factor. Proceedings of the National Academy of Sciences *90*, 8332-8336.
Serrano, A., Illgen, J., Brandt, U., Thieme, N., Letz, A., Lichius, A., Read, N.D., and Fleißner, A. (2018). Spatio-temporal MAPK dynamics mediate cell behavior coordination during fungal somatic cell fusion. Journal of cell science *131*.
Shimada, Y., Gulli, M.-P., and Peter, M. (2000). Nuclear sequestration of the exchange factor Cdc24 by Far1 regulates cell polarity during yeast mating. Nature cell biology *2*, 117-124.
Slaughter, B.D., Schwartz, J.W., and Li, R. (2007). Mapping dynamic protein interactions in MAP kinase signaling using live-cell fluorescence fluctuation spectroscopy and imaging. Proceedings of the National Academy of Sciences *104*,

20320-20325.
Slessareva, J.E., and Dohlman, H.G. (2006). G protein signaling in yeast: new components, new connections, new compartments. Science *314*, 1412-1413. 10.1126/science.1134041.
Sourjik, V., and Wingreen, N.S. (2012). Responding to chemical gradients: bacterial chemotaxis. Current opinion in cell biology *24*, 262-268.
St-Pierre, F., and Endy, D. (2008). Determination of cell fate selection during phage lambda infection. Proceedings of the National Academy of Sciences *105*, 20705-20710.
Sugiyama, M., Kaneko, Y., and Harashima, S. (2009). Yeast protein phosphatases Ptp2p and Msg5p are involved in G1–S transition, CLN2 transcription, and vacuole morphogenesis. Archives of microbiology *191*, 721-733.
Szczurek, E., Gat-Viks, I., Tiuryn, J., and Vingron, M. (2009). Elucidating regulatory mechanisms downstream of a signaling pathway using informative experiments. Molecular Systems Biology *5*, 287.
Takizawa, P.A., Sil, A., Swedlow, J.R., Herskowitz, I., and Vale, R.D. (1997). Actin-dependent localization of an RNA encoding a cell-fate determinant in yeast. Nature *389*, 90-93.
Treuner-Lange, A., and Sogaard-Andersen, L. (2014). Regulation of cell polarity in bacteria. J Cell Biol *206*, 7-17. 10.1083/jcb.201403136.
van Drogen, F., Stucke, V.M., Jorritsma, G., and Peter, M. (2001). MAP kinase dynamics in response to pheromones in budding yeast. Nature cell biology *3*, 1051-1059.
Van Kampen, N.G. (1992). Stochastic processes in physics and chemistry (Elsevier).
Vladimirov, N., and Sourjik, V. (2009). Chemotaxis: how bacteria use memory.
Wang, J. (2015). Landscape and flux theory of non-equilibrium dynamical systems with application to biology. Advances in Physics *64*, 1-137. 10.1080/00018732.2015.1037068.
Wang, J., Li, C., and Wang, E. (2010a). Potential and flux landscapes quantify the stability and robustness of budding yeast cell cycle network. Proceedings of the National Academy of Sciences *107*, 8195-8200.
Wang, J., Xu, L., and Wang, E. (2008a). Potential landscape and flux framework of nonequilibrium networks: robustness, dissipation, and coherence of biochemical oscillations. Proceedings of the National Academy of Sciences *105*, 12271-12276.
Wang, J., Zhang, K., and Wang, E. (2008b). Robustness and dissipation of mitogen-activated protein kinases signal transduction network: Underlying funneled landscape against stochastic fluctuations. The Journal of chemical physics *129*, 10B602.
Wang, J., Zhang, K., and Wang, E. (2010b). Kinetic paths, time scale, and underlying landscapes: A path integral framework to study global natures of nonequilibrium systems and networks. The Journal of chemical physics *133*, 09B613.
Wang, J., Zhang, K., Xu, L., and Wang, E. (2011). Quantifying the Waddington landscape and biological paths for development and differentiation. Proceedings of the National Academy of Sciences *108*, 8257-8262.
Wang, Y.Q., and Dohlman, H.G. (2004). Pheromone signaling mechanisms in yeast: A

prototypical sex machine. Science *306*, 1508-1509. DOI 10.1126/science.1104568.
Warringer, J., Zörgö, E., Cubillos, F.A., Zia, A., Gjuvsland, A., Simpson, J.T., Forsmark, A., Durbin, R., Omholt, S.W., and Louis, E.J. (2011). Trait variation in yeast is defined by population history. PLoS Genet *7*, e1002111.
White, J.M., and Rose, M.D. (2001). Yeast mating: getting close to membrane merger. Current biology *11*, R16-R20.
Winters, M.J., Lamson, R.E., Nakanishi, H., Neiman, A.M., and Pryciak, P.M. (2005). A membrane binding domain in the Ste5 scaffold synergizes with Gβγ binding to control localization and signaling in pheromone response. Molecular cell *20*, 21-32.
Xu, F., Bierman, R., Healy, F., and Nguyen, H. (2016). A multi-scale model of Escherichia coli chemotaxis from intracellular signaling pathway to motility and nutrient uptake in nutrient gradient and isotropic fluid environments. Computers & Mathematics with Applications *71*, 2466-2478.
Yosef, N., and Regev, A. (2011). Impulse Control: Temporal Dynamics in Gene Transcription. Cell *144*, 886-896. 10.1016/j.cell.2011.02.015.
Youk, H., and Lim, W.A. (2014a). Secreting and sensing the same molecule allows cells to achieve versatile social behaviors. Science *343*, 1242782.
Youk, H., and Lim, W.A. (2014b). Secreting and Sensing the Same Molecule Allows Cells to Achieve Versatile Social Behaviors. Science *343*, 628-+. ARTN 1242782 10.1126/science.1242782.
Yuan, J., Fahrner, K.A., Turner, L., and Berg, H.C. (2010). Asymmetry in the clockwise and counterclockwise rotation of the bacterial flagellar motor. Proceedings of the National Academy of Sciences *107*, 12846-12849.
Zeng, L., Skinner, S.O., Zong, C., Sippy, J., Feiss, M., and Golding, I. (2010). Decision making at a subcellular level determines the outcome of bacteriophage infection. Cell *141*, 682-691.
Zheng, W., Zhao, H., Mancera, E., Steinmetz, L.M., and Snyder, M. (2010). Genetic analysis of variation in transcription factor binding in yeast. Nature *464*, 1187-1191.
Zhou, P.J., Gao, X., Li, X.L., Li, L.X., Niu, C.Y., Ouyang, Q., Lou, H.Q., Li, T.J., and Li, F.T. (2021). Stochasticity Triggers Activation of the S-phase Checkpoint Pathway in Budding Yeast. Physical Review X *11*. ARTN 011004 10.1103/PhysRevX.11.011004.
Zörgö, E., Chwialkowska, K., Gjuvsland, A.B., Garré, E., Sunnerhagen, P., Liti, G., Blomberg, A., Omholt, S.W., and Warringer, J. (2013). Ancient evolutionary trade-offs between yeast ploidy states. PLoS Genet *9*, e1003388.

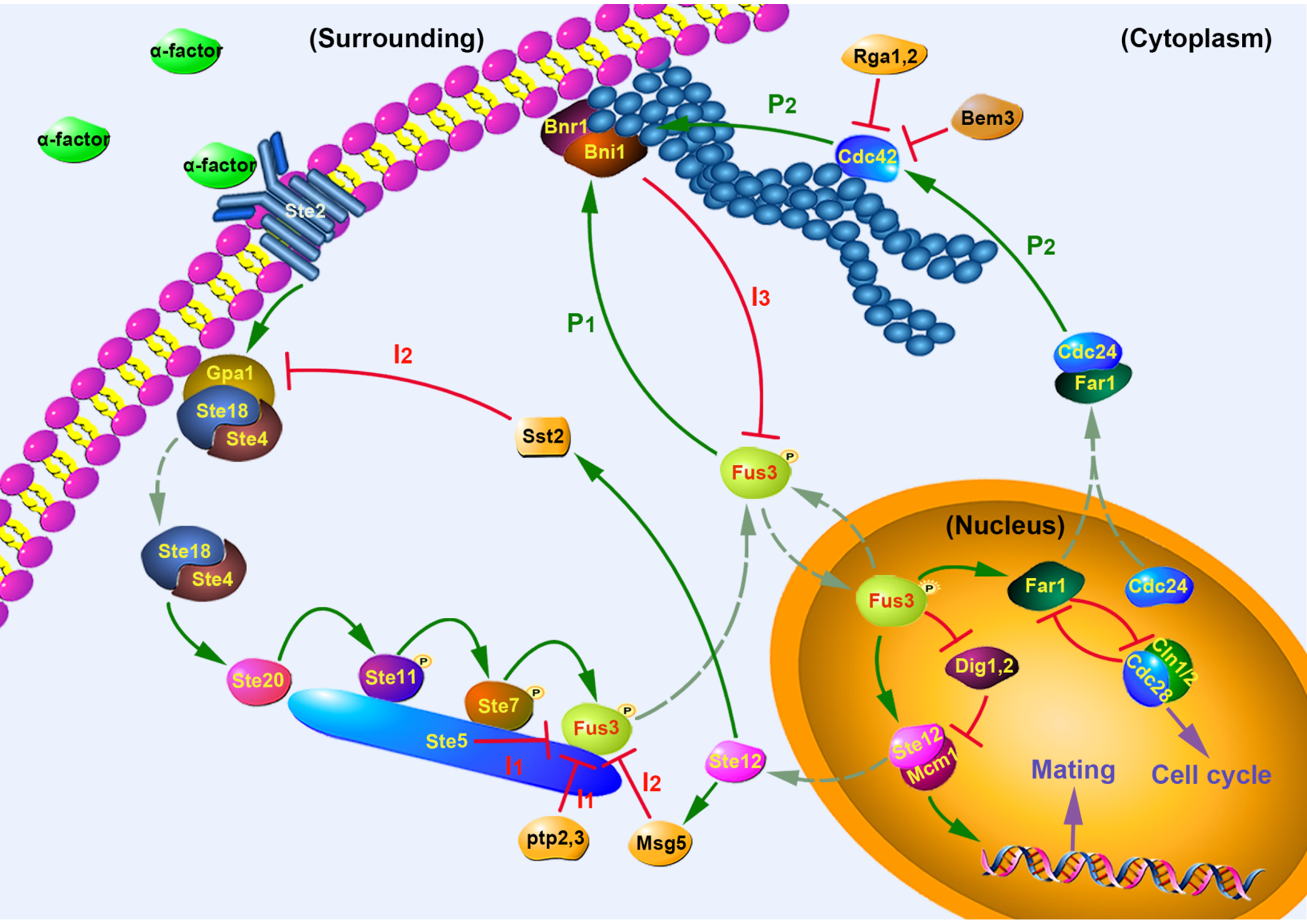

(Surrounding)
(Cytoplasm)
α-factor
α-factor
α-factor
Ste2
Gpa1
Ste18
Ste4
Ste18
Ste4
Ste20
Ste11
Ste7
Fus3
Ste5
I1
I1
I2
ptp2,3
Msg5
Ste12
Sst2
I2
P1
I3
Bnr1
Bni1
P2
Rga1,2
Bem3
Cdc42
P2
Cdc24
Far1
Fus3
(Nucleus)
Fus3
Far1
Cdc24
Dig1,2
Cln1/2
Cdc28
Ste12
Mcm1
Mating
Cell cycle

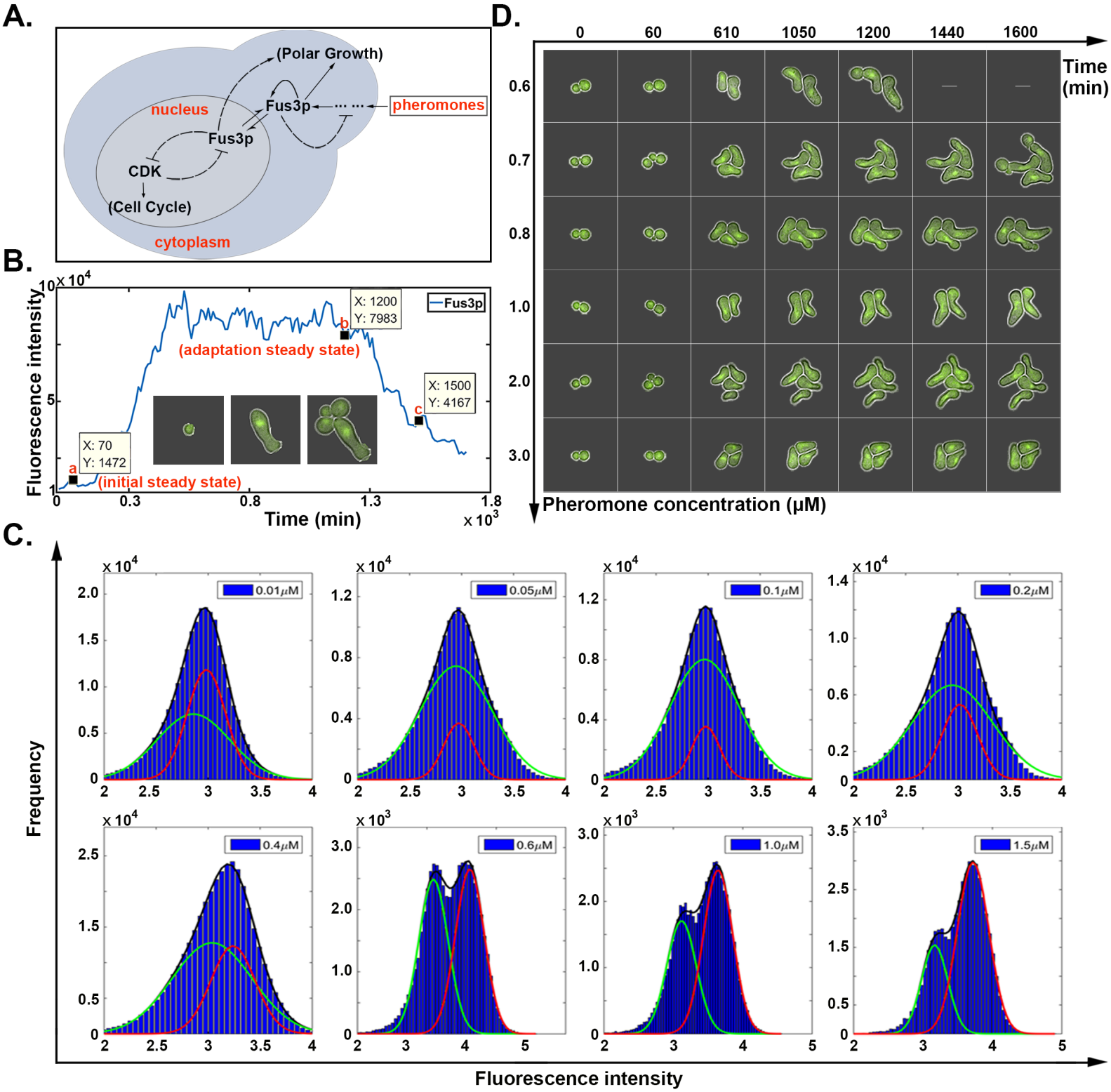
A.
(Polar Growth)
nucleus
Fus3p
pheromones
Fus3p
CDK
(Cell Cycle)
cytoplasm
B.
Fluorescence intensity
x 10^4
Fus3p
X: 1200
Y: 7983
(adaptation steady state)
X: 1500
Y: 4167
X: 70
Y: 1472
(initial steady state)
Time (min)
x 10^3
D.
0
60
610
1050
1200
1440
1600
Time (min)
0.6
0.7
0.8
1.0
2.0
3.0
Pheromone concentration (μM)
C.
Frequency
0.01μM
0.05μM
0.1μM
0.2μM
0.4μM
0.6μM
1.0μM
1.5μM
Fluorescence intensity

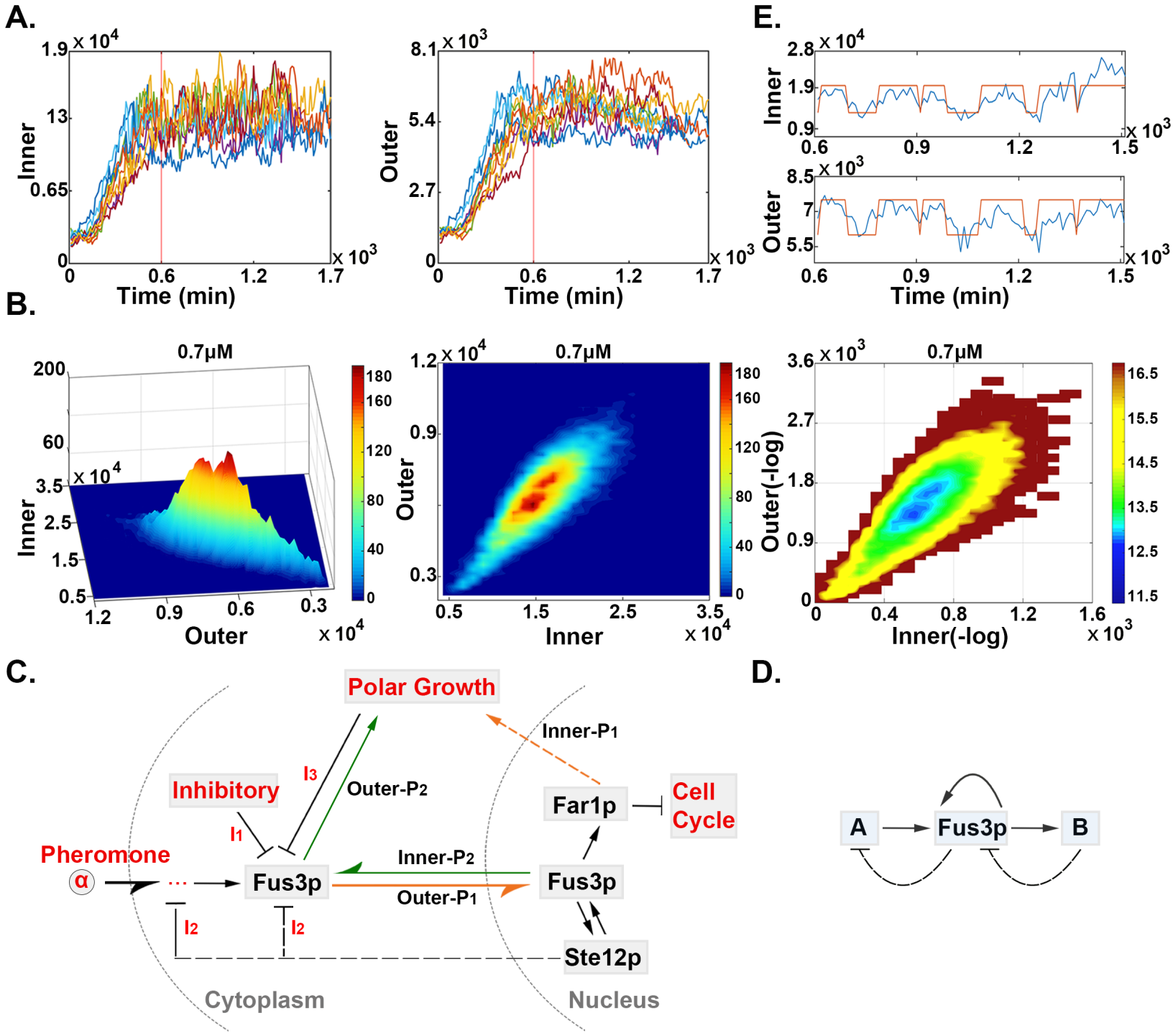
A.
Inner
Time (min)
Outer
Time (min)
E.
Inner
Outer
Time (min)
B.
0.7μM
Inner
Outer
0.7μM
Inner
Outer
0.7μM
Outer(-log)
Inner(-log)
C.
Polar Growth
Inner-P1
Inhibitory
I3
Outer-P2
Far1p
Cell Cycle
Pheromone
α
I1
Fus3p
Inner-P2
Outer-P1
Fus3p
I2
I2
Ste12p
Cytoplasm
Nucleus
D.
A
Fus3p
B

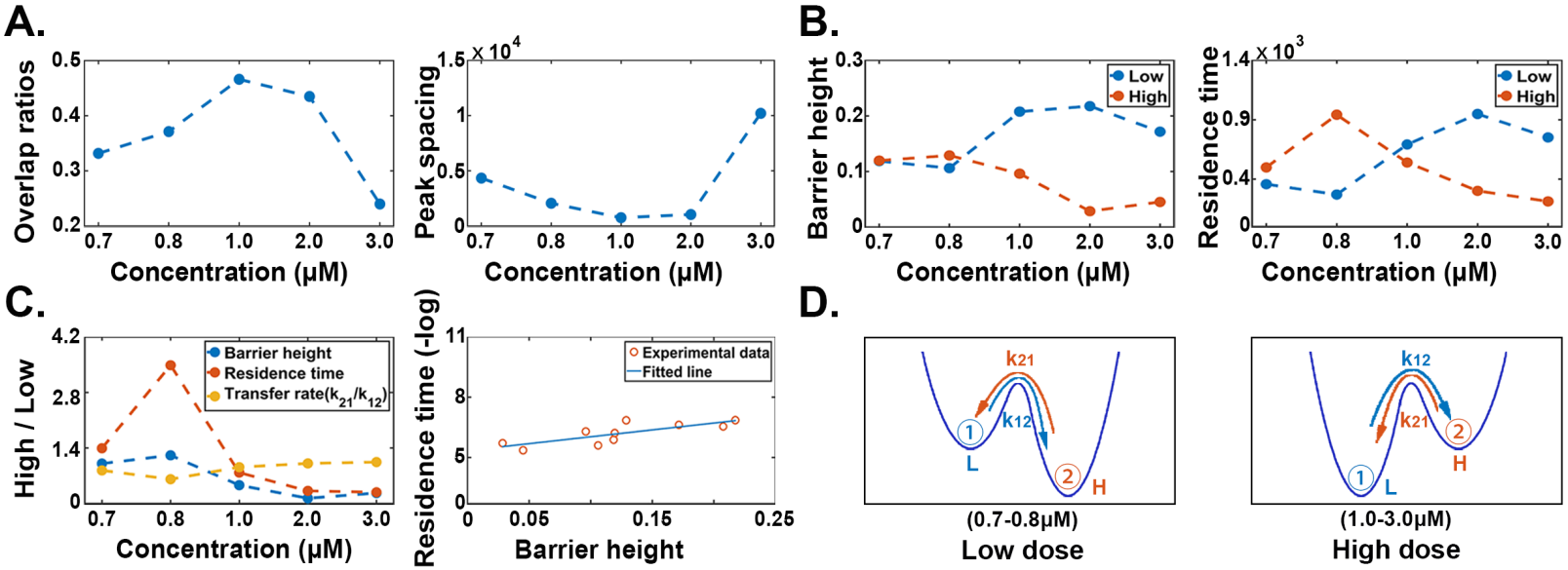
A.
Overlap ratios
Concentration (μM)
Peak spacing
x 10^4
Concentration (μM)
B.
Barrier height
Low
High
Concentration (μM)
Residence time
x 10^3
Low
High
Concentration (μM)
C.
High / Low
Barrier height
Residence time
Transfer rate(k21/k12)
Concentration (μM)
Residence time (-log)
Experimental data
Fitted line
Barrier height
D.
k21
k12
L
H
(0.7-0.8μM)
Low dose
k12
k21
L
H
(1.0-3.0μM)
High dose

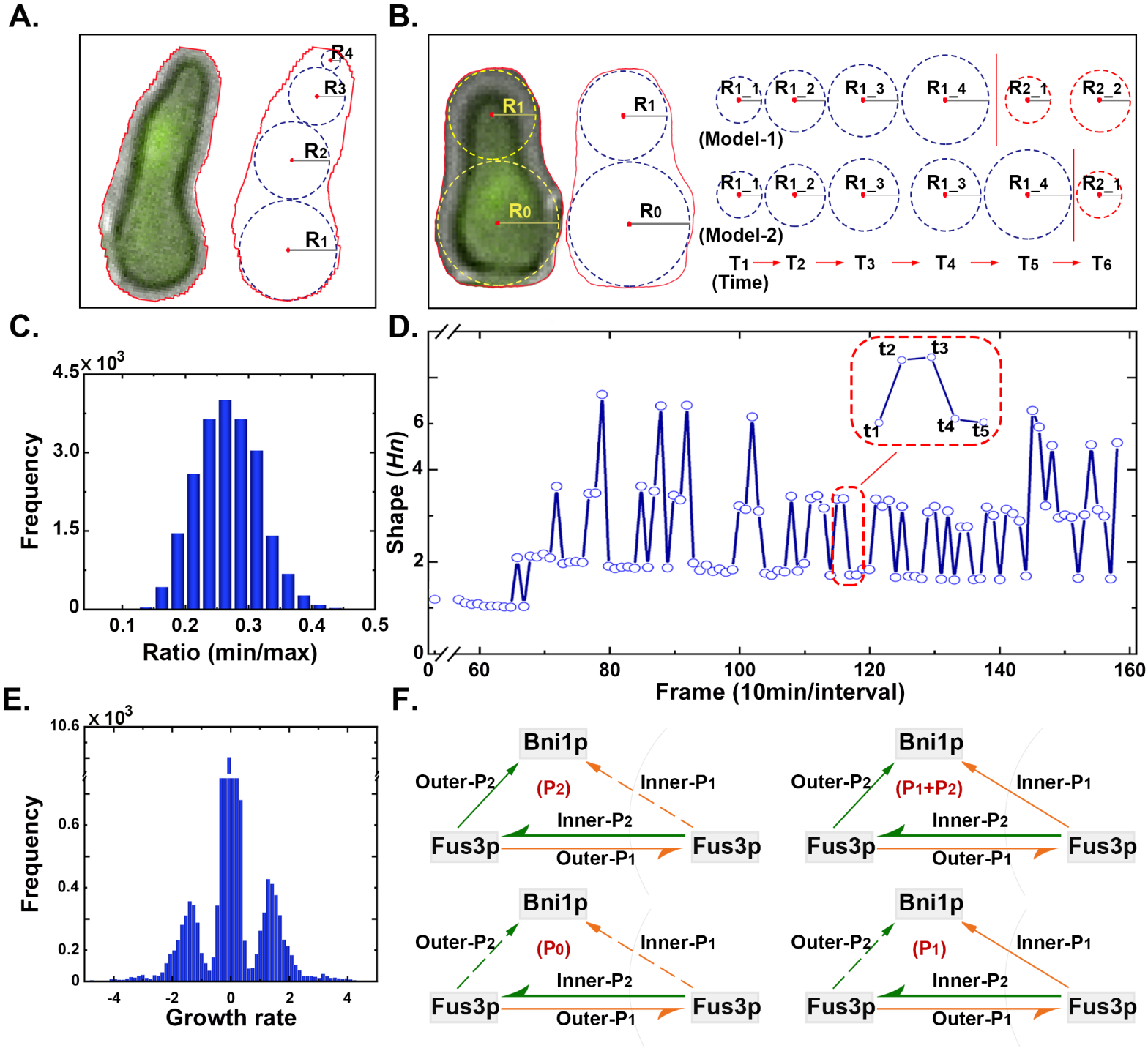
A.
R4
R3
R2
R1
B.
R1
R0
R1
R0
R1_1
R1_2
R1_3
R1_4
R2_1
R2_2
(Model-1)
R1_1
R1_2
R1_3
R1_3
R1_4
R2_1
(Model-2)
T1
T2
T3
T4
T5
T6
(Time)
C.
x 10^3
4.5
3.0
1.5
0
Frequency
0.1
0.2
0.3
0.4
0.5
Ratio (min/max)
D.
t2
t3
t1
t4
t5
Shape (Hn)
0
2
4
6
0
60
80
100
120
140
160
Frame (10min/interval)
E.
x 10^3
10.6
0.6
0.4
0.2
0
Frequency
-4
-2
0
2
4
Growth rate
F.
Bni1p
Outer-P2
(P2)
Inner-P1
Inner-P2
Fus3p
Outer-P1
Fus3p
Bni1p
Outer-P2
(P1+P2)
Inner-P1
Inner-P2
Fus3p
Outer-P1
Fus3p
Bni1p
Outer-P2
(P0)
Inner-P1
Inner-P2
Fus3p
Outer-P1
Fus3p
Bni1p
Outer-P2
(P1)
Inner-P1
Inner-P2
Fus3p
Outer-P1
Fus3p

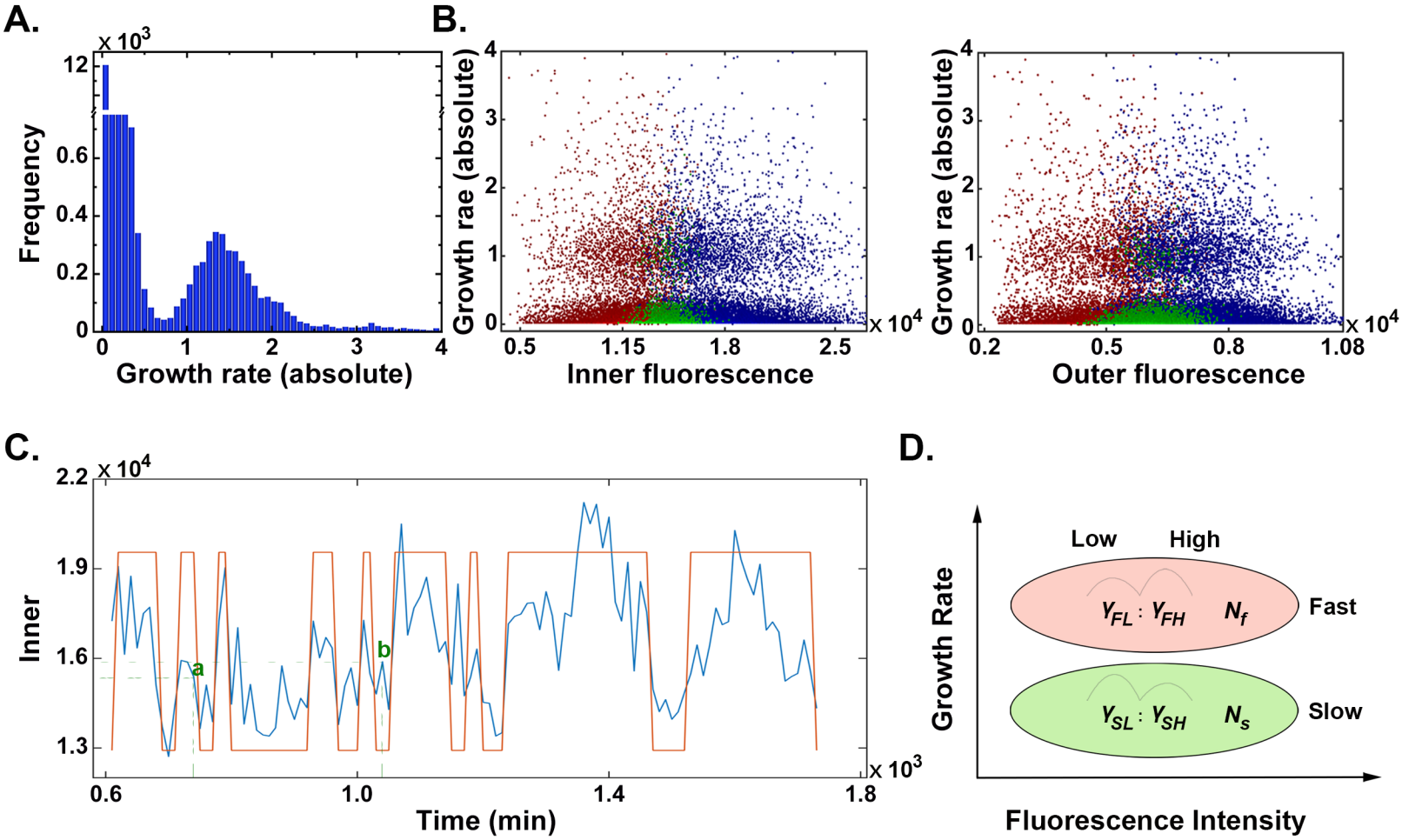
A.
x 10^3
12
0.6
0.4
0.2
0
Frequency
0
1
2
3
4
Growth rate (absolute)
B.
Growth rae (absolute)
4
3
2
1
0
0.5
1.15
1.8
2.5
x 10^4
Inner fluorescence
Growth rae (absolute)
0.2
0.5
0.8
1.08
x 10^4
Outer fluorescence
C.
x 10^4
2.2
1.9
1.6
1.3
Inner
a
b
0.6
1.0
1.4
1.8
x 10^3
Time (min)
D.
Low
High
Growth Rate
Y_{FL} : Y_{FH}
N_f
Fast
Y_{SL} : Y_{SH}
N_s
Slow
Fluorescence Intensity

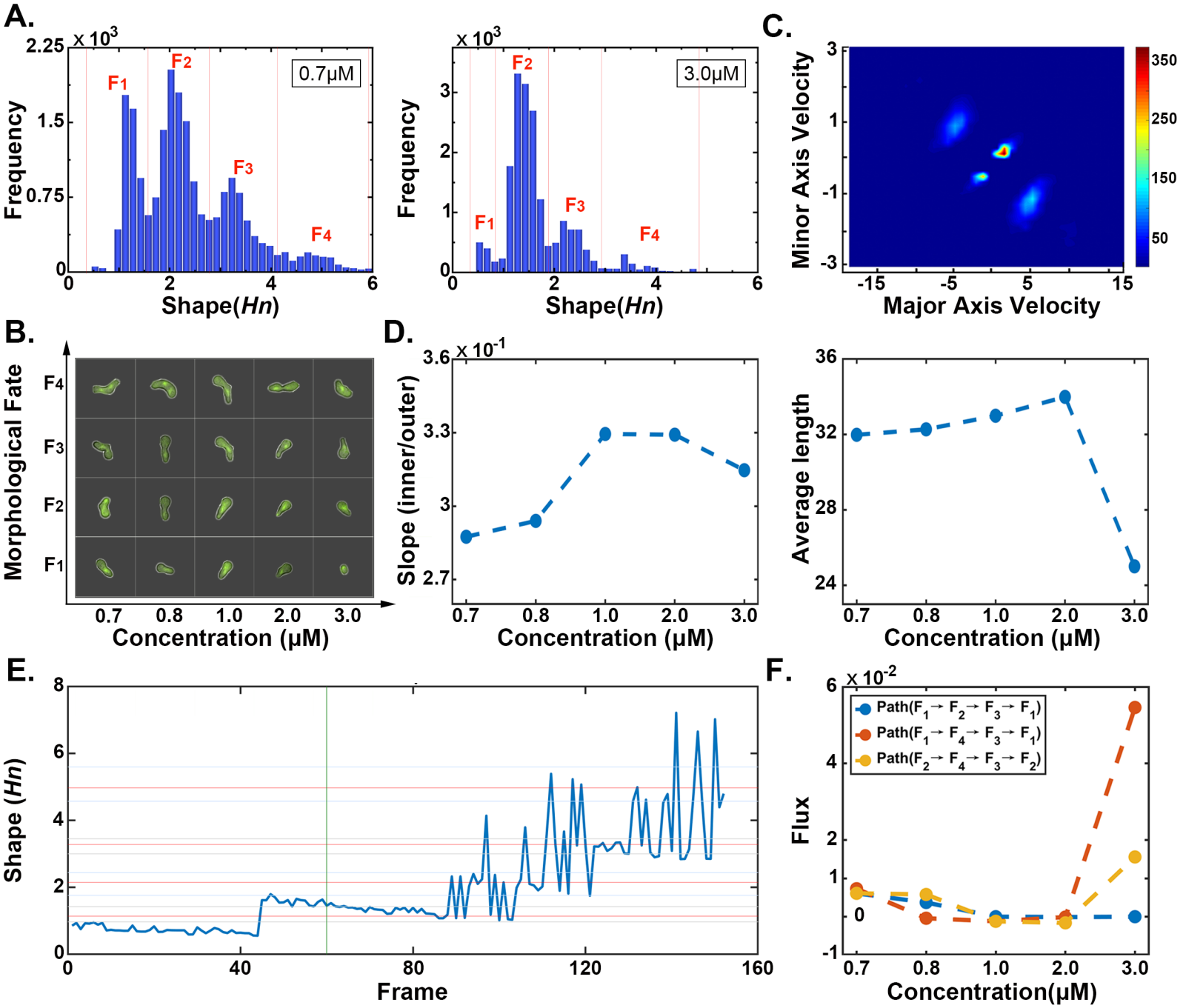
A.
x 10^3
0.7μM
F1
F2
F3
F4
Frequency
Shape(Hn)
3.0μM
B.
Morphological Fate
Concentration (μM)
C.
Minor Axis Velocity
Major Axis Velocity
D.
x 10^-1
Slope (inner/outer)
Average length
E.
Shape (Hn)
Frame
F.
x 10^-2
Path(F1→ F2→ F3→ F1)
Path(F1→ F4→ F3→ F1)
Path(F2→ F4→ F3→ F2)
Flux
Concentration(μM)

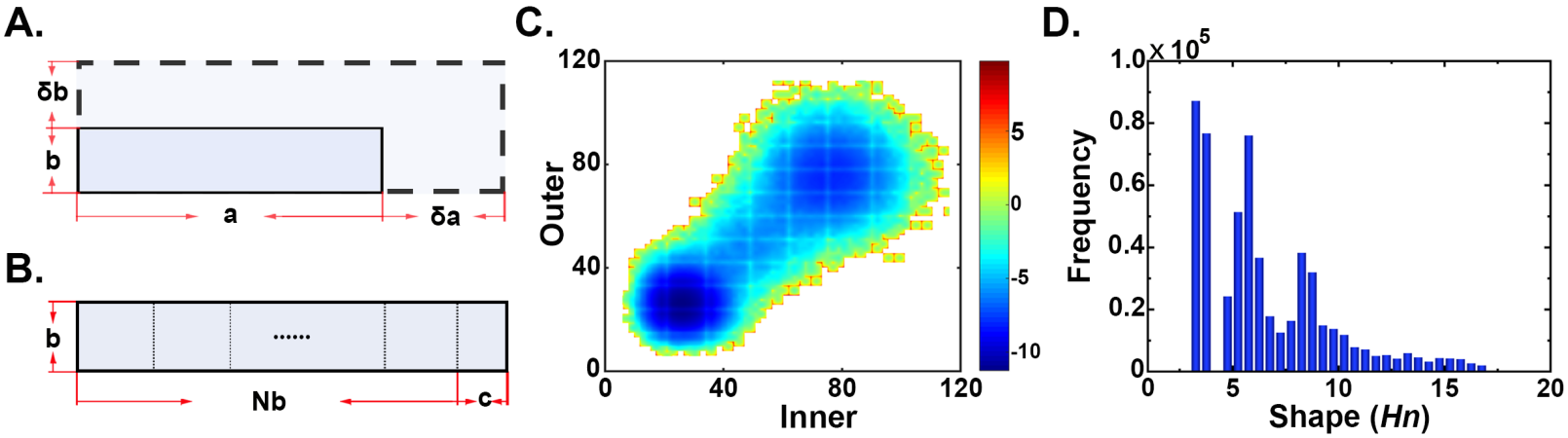
A.
δb
b
a
δa
B.
b
.....
Nb
c
C.
Outer
Inner
0
40
80
120
5
0
-5
-10
D.
Frequency
Shape (Hn)
1.0
0.8
0.6
0.4
0.2
0
5
10
15
20
X 10^5

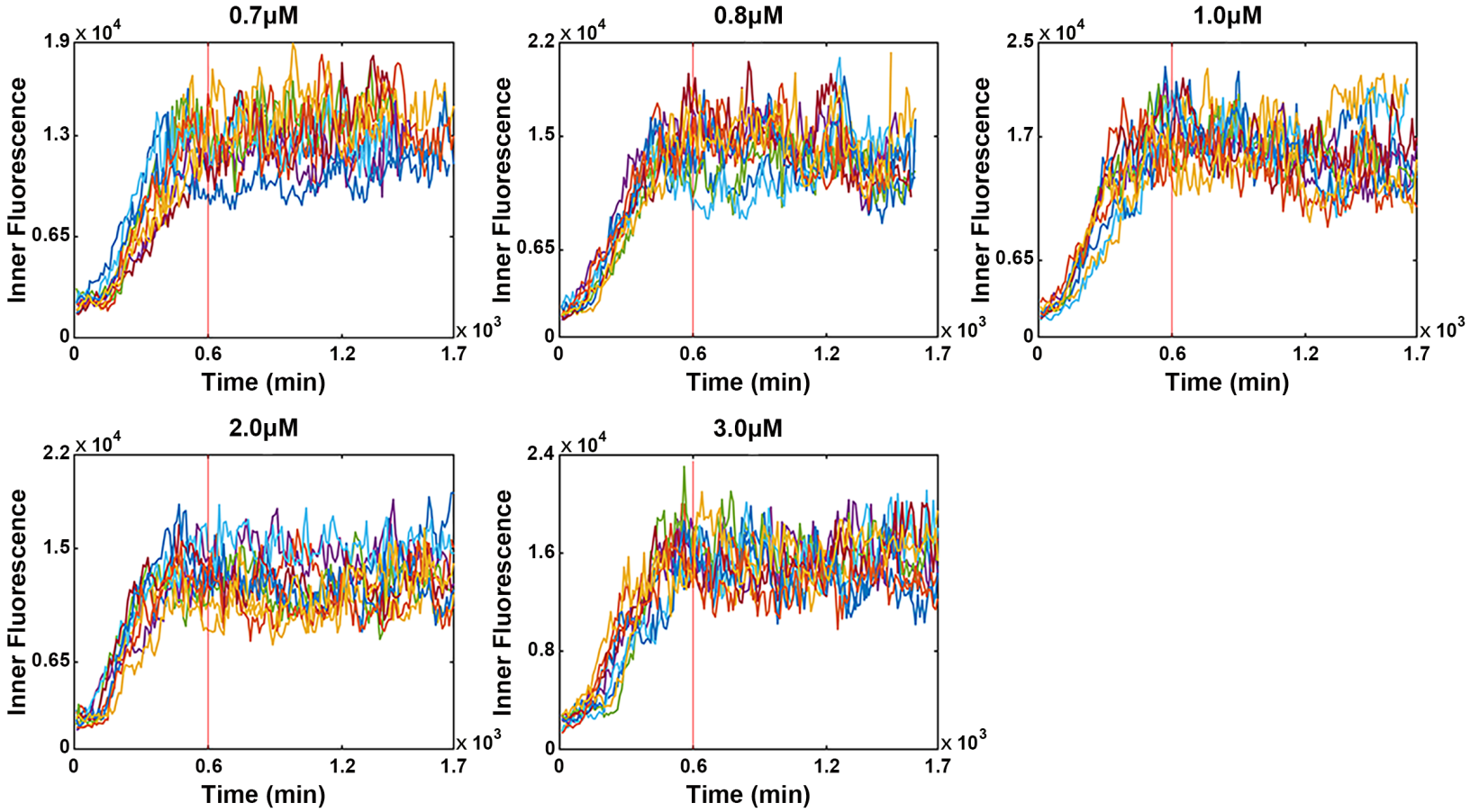
0.7μM
0.8μM
1.0μM
2.0μM
3.0μM
Inner Fluorescence
Time (min)
x 10^4
x 10^3
0
0.6
1.2
1.7
0.65
1.3
1.9
1.5
2.2
2.5
1.7
0.8
1.6
2.4

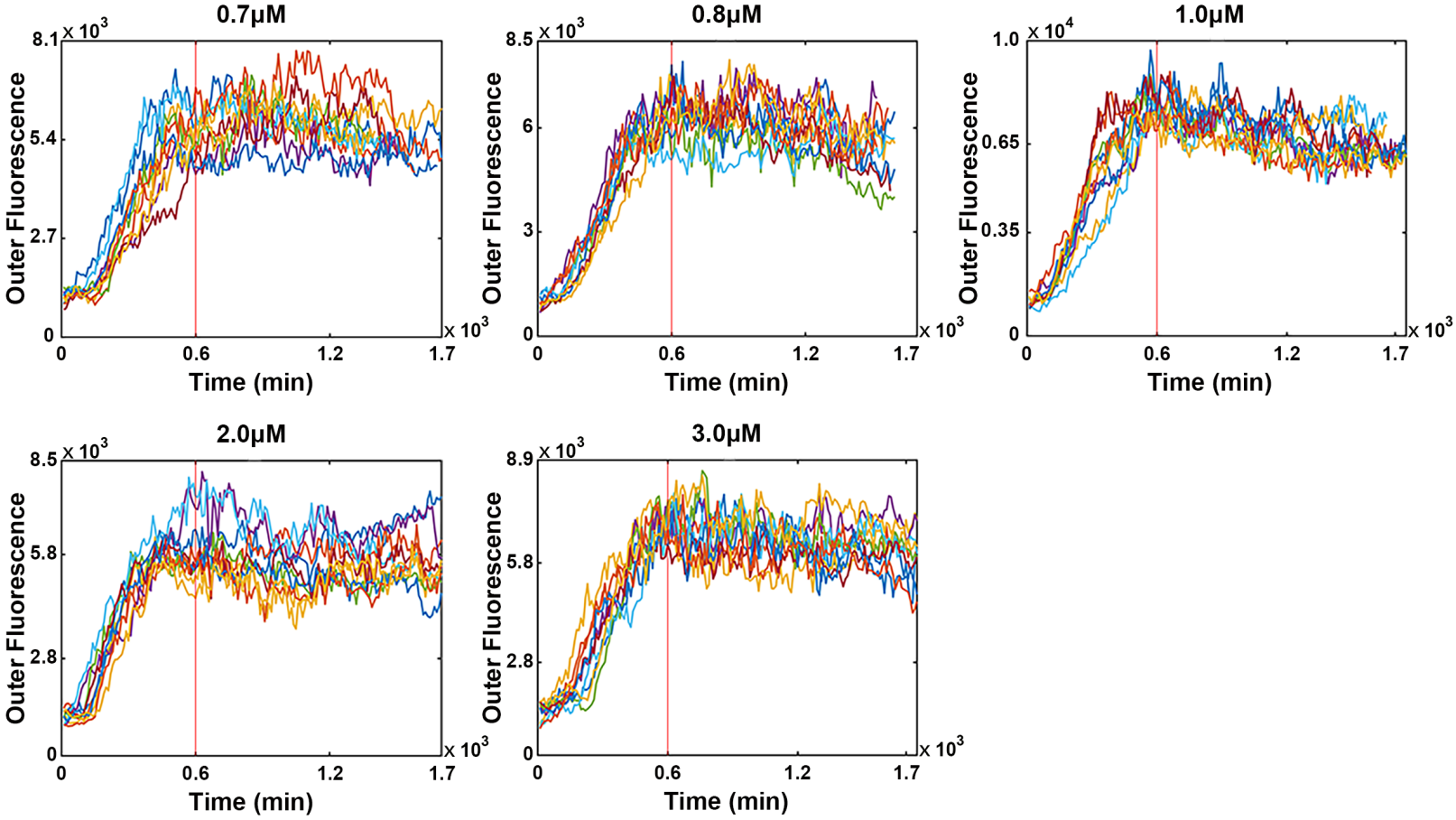
0.7μM
0.8μM
1.0μM
2.0μM
3.0μM
Outer Fluorescence
Time (min)
x 10^3
x 10^4
0
0.6
1.2
1.7
8.1
5.4
2.7
8.5
6
3
1.0
0.65
0.35
5.8
2.8
8.9

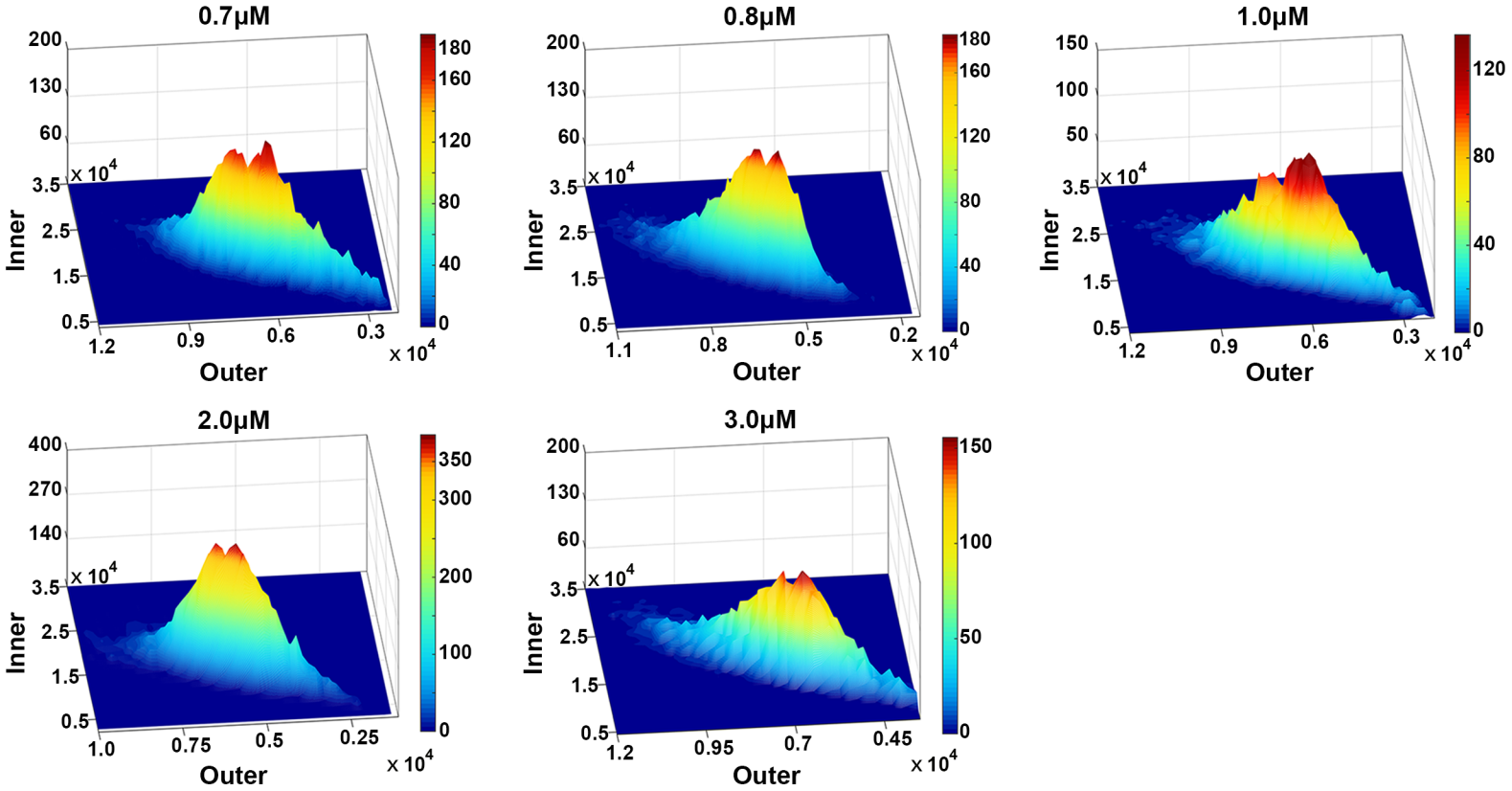
0.7μM
0.8μM
1.0μM
2.0μM
3.0μM
Inner
Outer
x 10^4

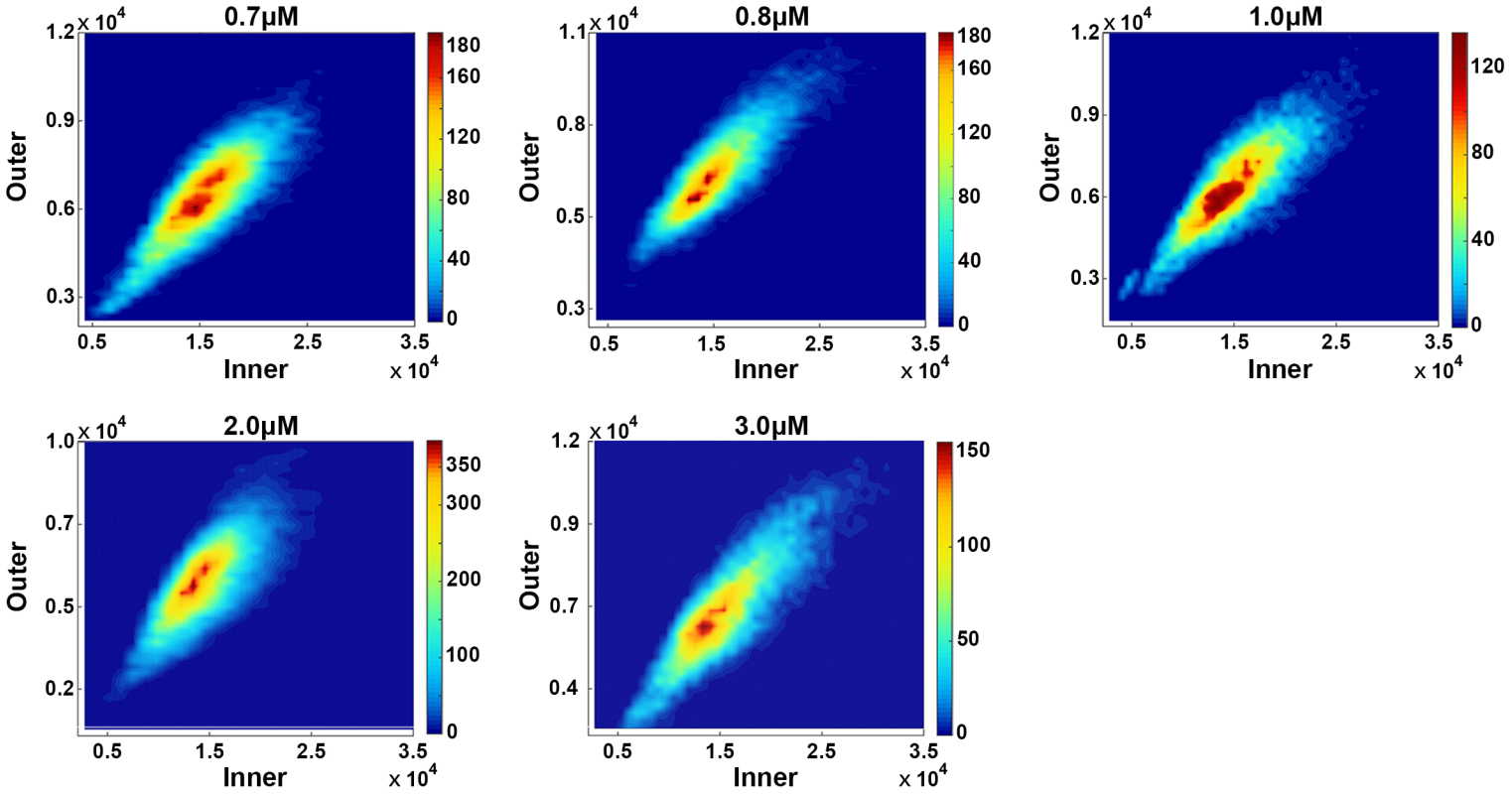
0.7μM
0.8μM
1.0μM
2.0μM
3.0μM
Outer
Inner
x 10^4

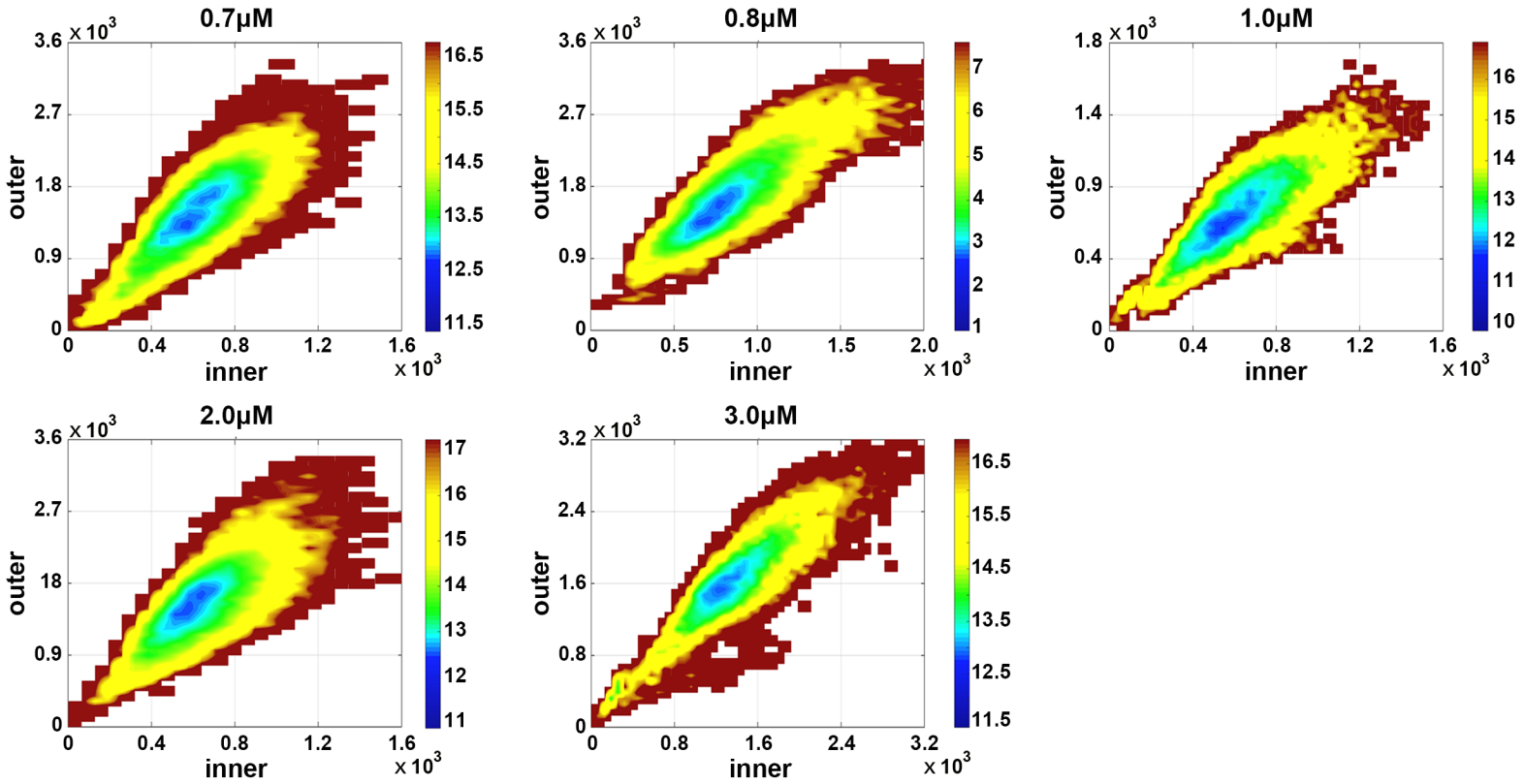
0.7μM
0.8μM
1.0μM
2.0μM
3.0μM
outer
inner
x 10^3

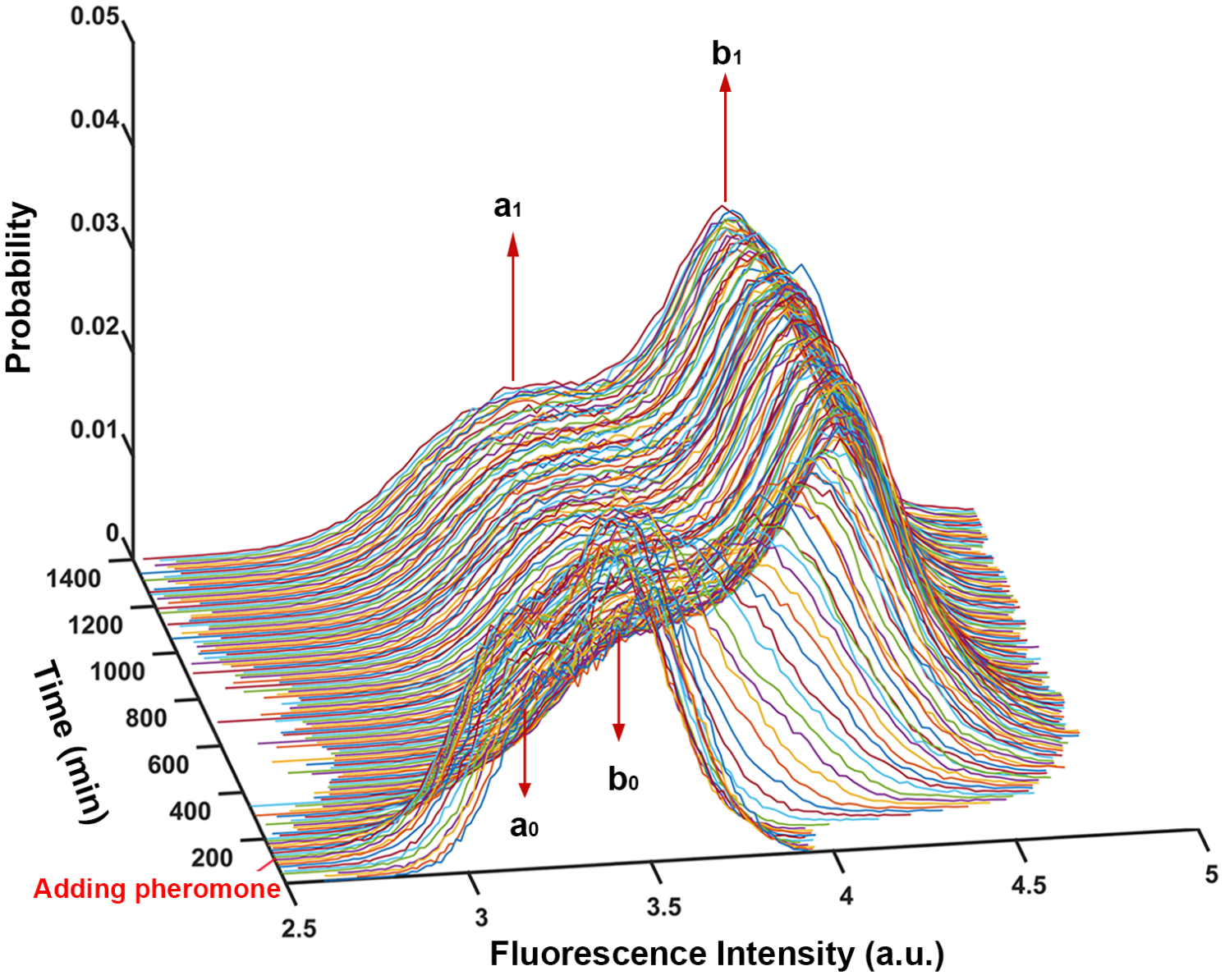
Probability
0.05
0.04
0.03
0.02
0.01
0
Time (min)
1400
1200
1000
800
600
400
200
Adding pheromone
2.5
3
3.5
4
4.5
5
Fluorescence Intensity (a.u.)
a1
b1
a0
b0

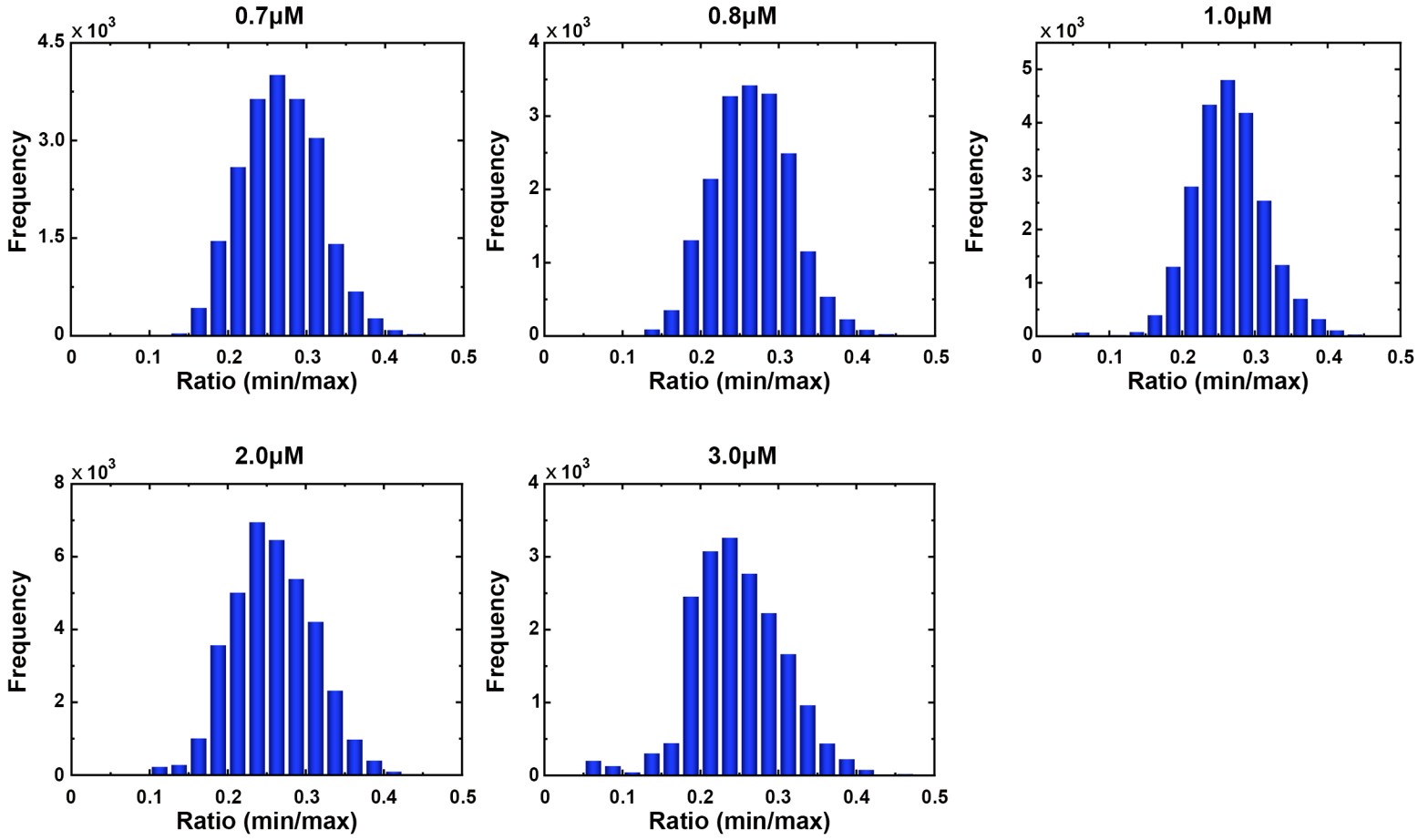
0.7μM
0.8μM
1.0μM
2.0μM
3.0μM
x 10^3
Frequency
Ratio (min/max)

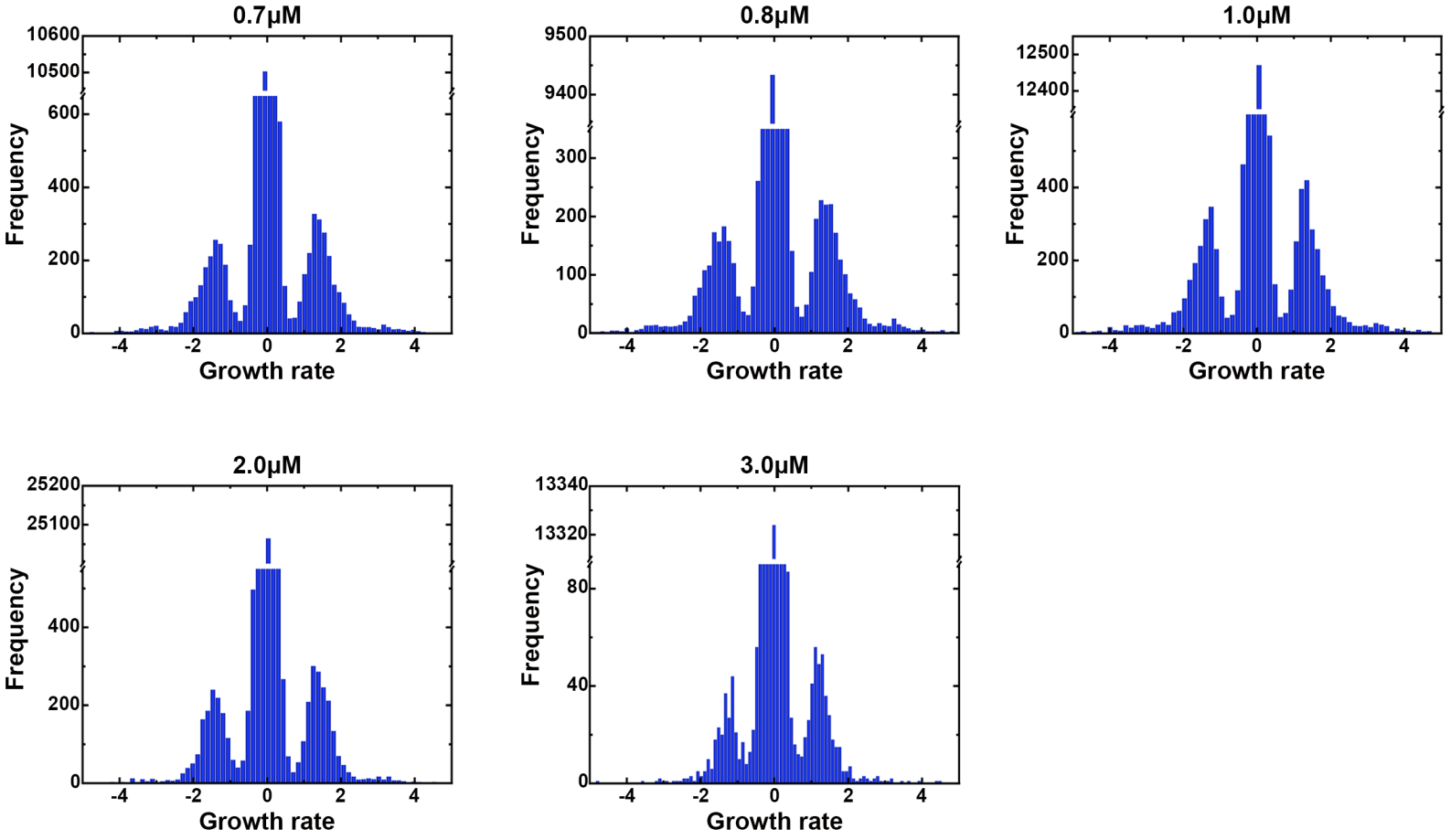
0.7μM
0.8μM
1.0μM
2.0μM
3.0μM
Frequency
Growth rate
10600
10500
600
400
200
0
9500
9400
300
200
100
12500
12400
25200
25100
13340
13320
80
40
-4
-2
0
2
4

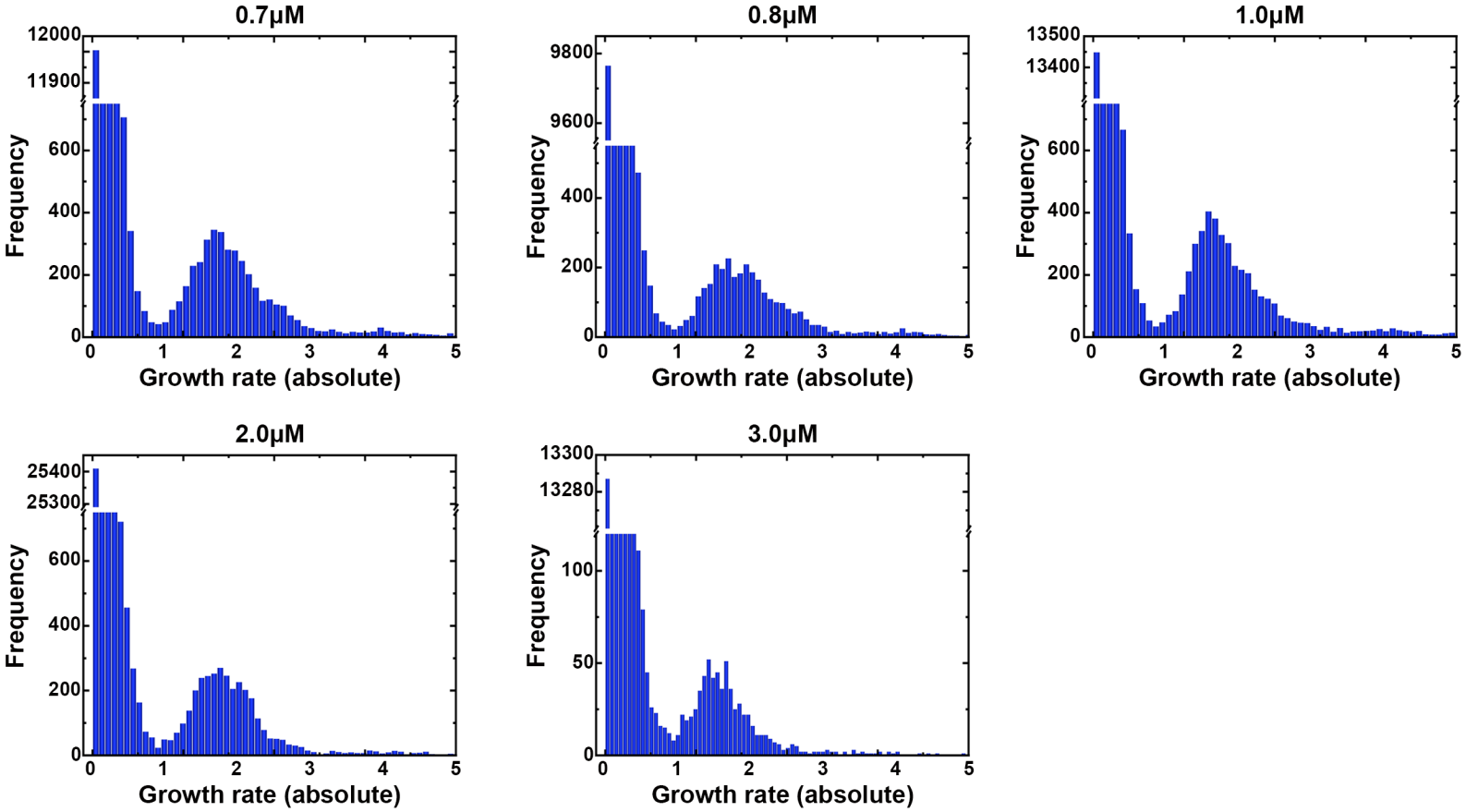
0.7μM
0.8μM
1.0μM
2.0μM
3.0μM
Frequency
Growth rate (absolute)
12000
11900
600
400
200
0
9800
9600
13500
13400
25400
25300
13300
13280
100
50
1
2
3
4
5

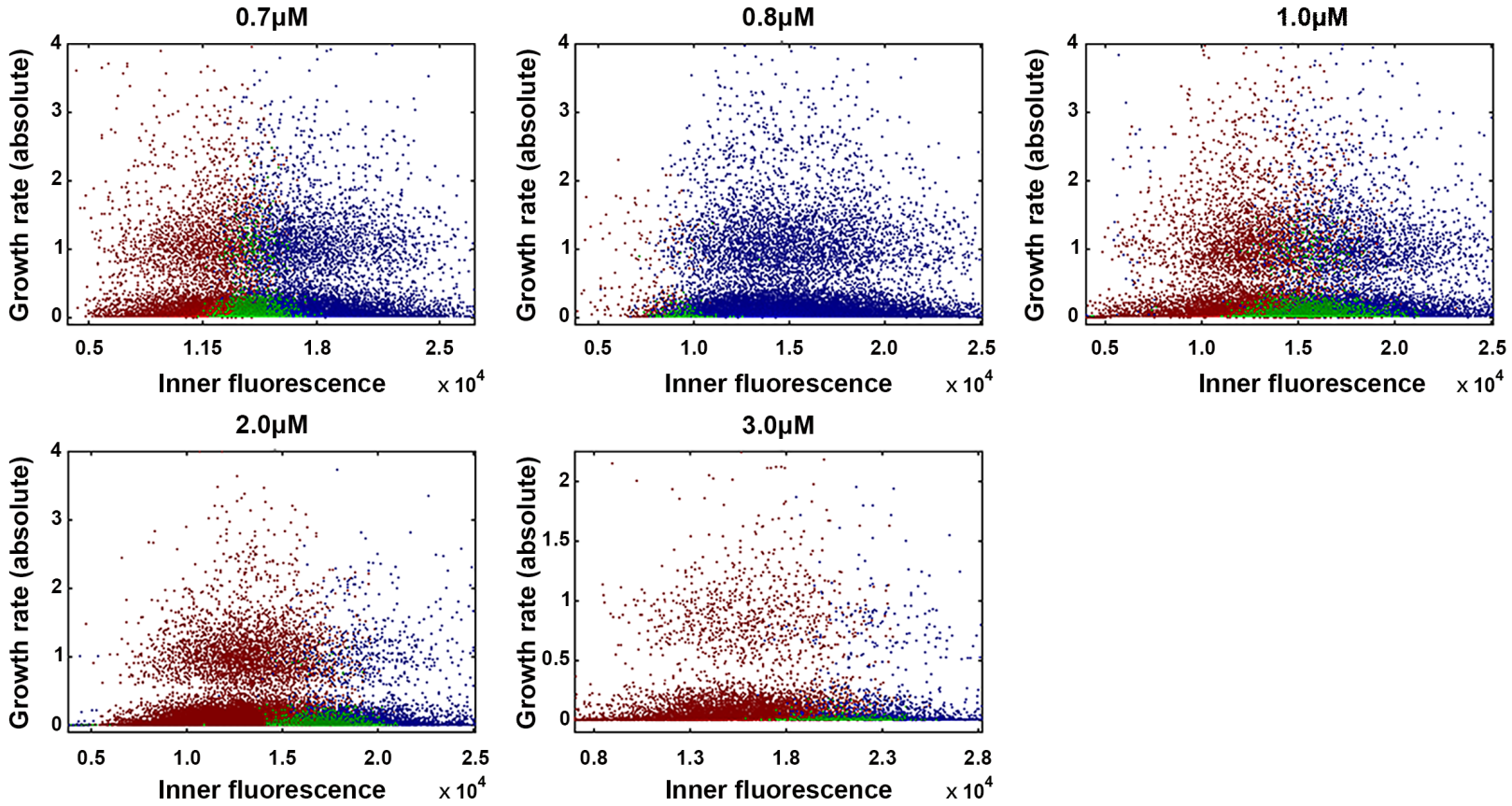
0.7μM
0.8μM
1.0μM
2.0μM
3.0μM
Growth rate (absolute)
Inner fluorescence
x 10^4
0.5
1.15
1.8
2.5
1.0
1.5
2.0
0.8
1.3
2.3
2.8
0
0.5
1
1.5
2
3
4

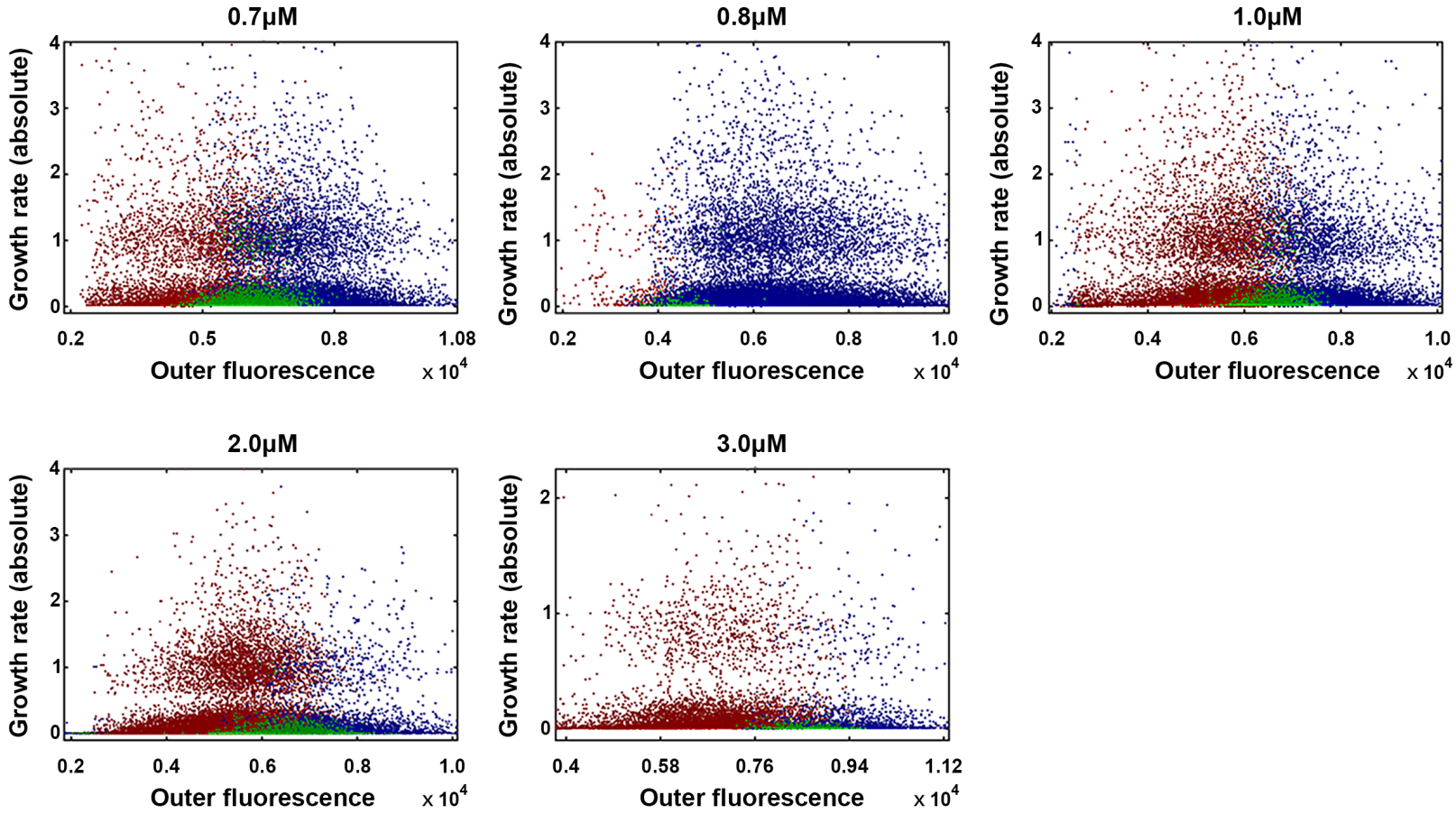
0.7μM
0.8μM
1.0μM
2.0μM
3.0μM
Growth rate (absolute)
Outer fluorescence
x 10^4
0.2
0.5
0.8
1.08
0.4
0.6
1.0
0.58
0.76
0.94
1.12
0
1
2
3
4

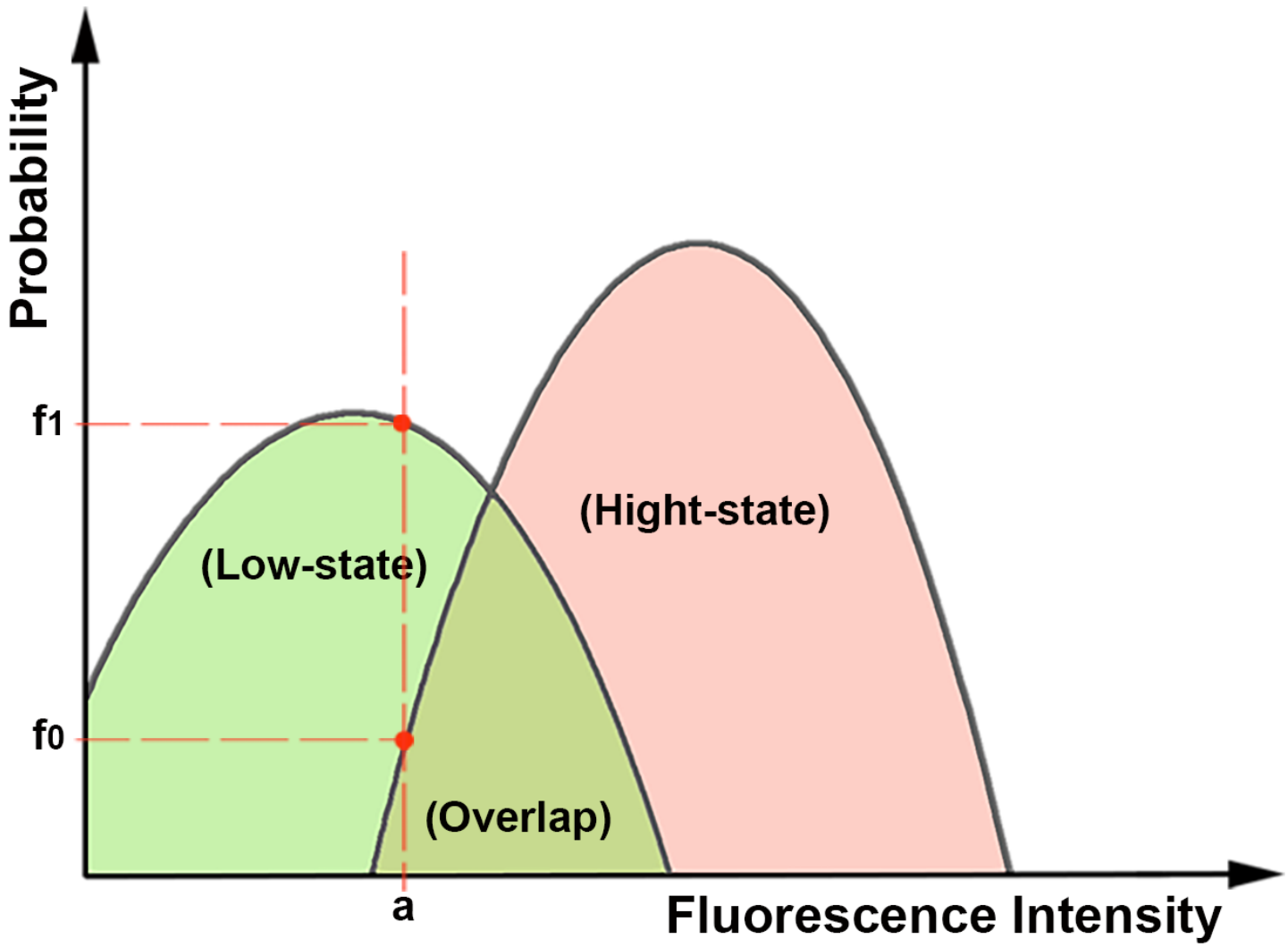
Probability
f1
f0
(Low-state)
(Hight-state)
(Overlap)
a
Fluorescence Intensity

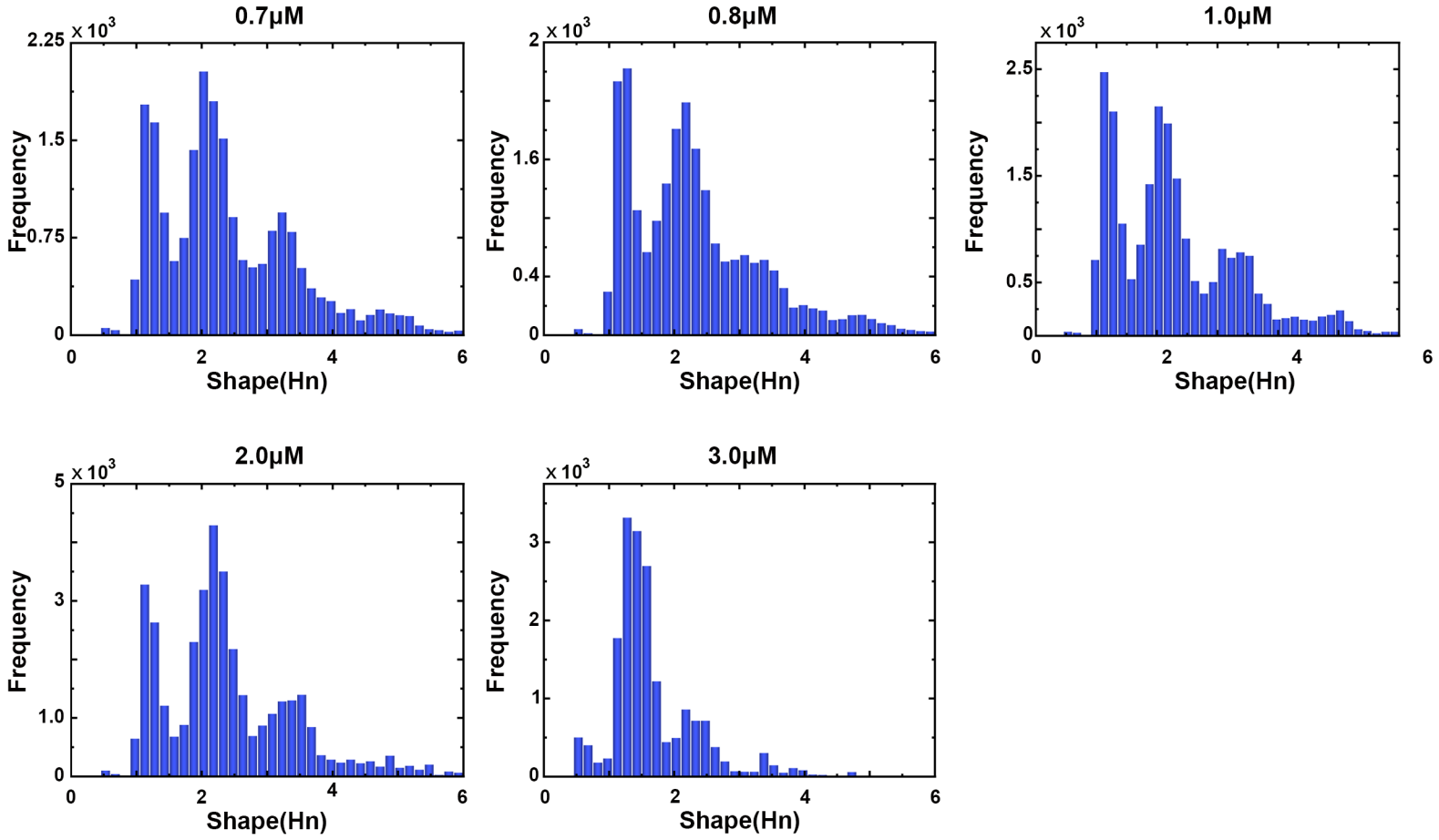
0.7μM
0.8μM
1.0μM
2.0μM
3.0μM
x 10^3
Frequency
Shape(Hn)

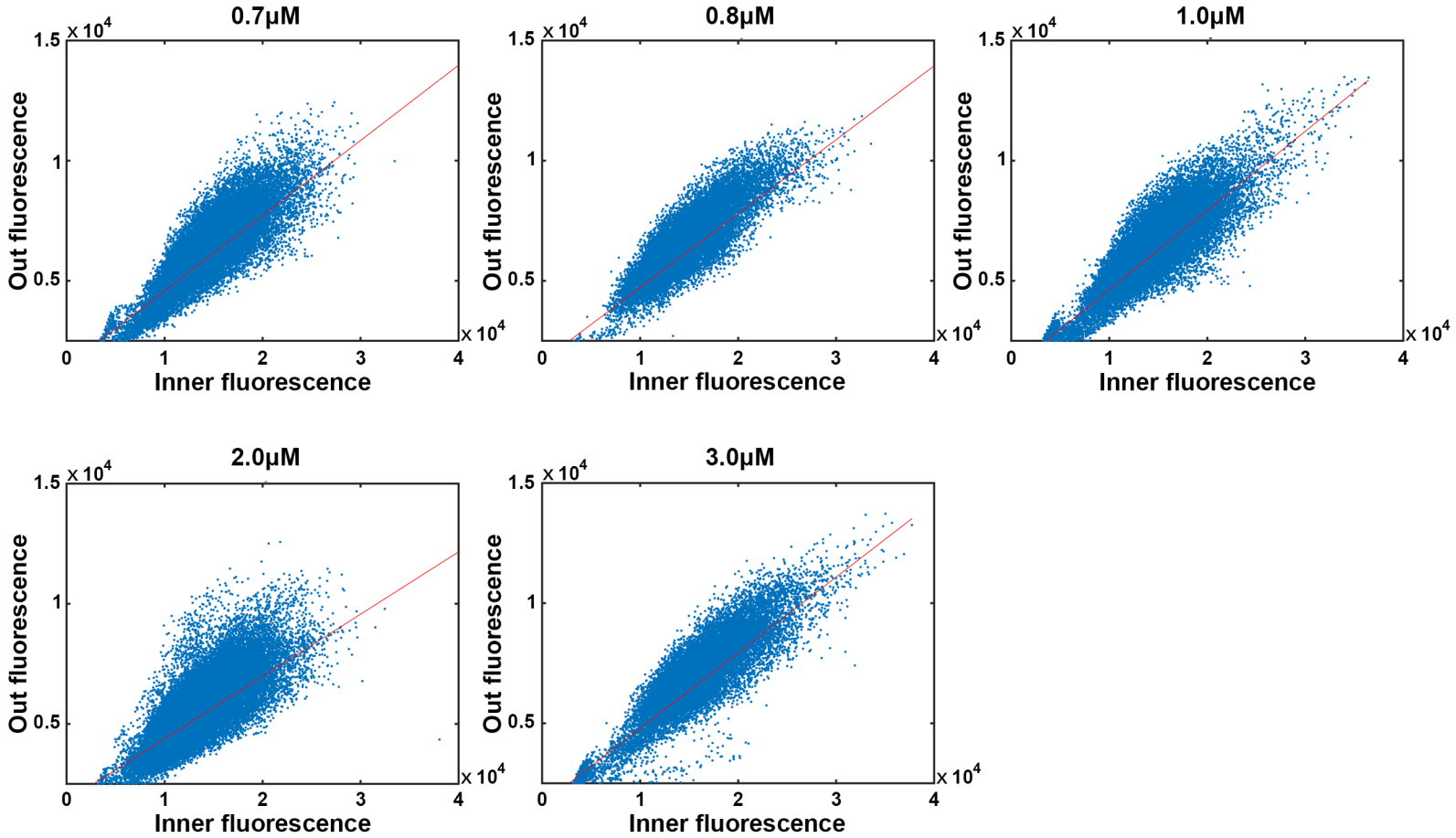
0.7μM
0.8μM
1.0μM
2.0μM
3.0μM
Out fluorescence
Inner fluorescence
x 10^4
1.5
1
0.5
0
1
2
3
4